Extending the Lifetime of Organic Flow Batteries via Redox State Management

Marc-Antoni Goulet,[†,‖,⊥] Liuchuan Tong,[‡,‖] Daniel A. Pollack,[§] Daniel P. Tabor,[‡] Susan A. Odom,[†,∇] Alán Aspuru-Guzik,[‡,¶] Eugene E. Kwan,*[‡] Roy G. Gordon,*[†,‡] and Michael J. Aziz*[†]

[†]Harvard John A. Paulson School of Engineering and Applied Sciences, Harvard University, Cambridge, Massachusetts 02138, United States

[‡]Department of Chemistry and Chemical Biology, Harvard University, Cambridge, Massachusetts 02138, United States

[§]Department of Physics, Harvard University, Cambridge, Massachusetts 02138, United States

[∇]Department of Chemistry, University of Kentucky, Lexington, Kentucky 40506, United States

Ⓢ *Supporting Information*

ABSTRACT: Redox flow batteries based on quinone-bearing aqueous electrolytes have emerged as promising systems for energy storage from intermittent renewable sources. The lifetime of these batteries is limited by quinone stability. Here, we confirm that 2,6-dihydroxyanthrahydroquinone tends to form an anthrone intermediate that is vulnerable to subsequent irreversible dimerization. We demonstrate quantitatively that this decomposition pathway is responsible for the loss of battery capacity. Computational studies indicate that the driving force for anthrone formation is greater for anthraquinones with lower reduction potentials. We show that the decomposition can be substantially mitigated. We demonstrate that conditions minimizing anthrone formation and avoiding anthrone dimerization slow the capacity loss rate by over an order of magnitude. We anticipate that this mitigation strategy readily extends to other anthraquinone-based flow batteries and is thus an important step toward realizing renewable electricity storage through long-lived organic flow batteries.
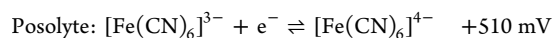
The cost of electricity generated from renewable sources such as the sun and wind has become competitive with electricity derived from fossil fuels.[1] Nonetheless, the widespread adoption of intermittent renewable electricity requires new methods for the reliable storage and delivery of electricity over long periods when these sources are unavailable for generation.[2−4] Redox flow batteries (RFBs), whose energy and power capabilities can be scaled independently, may enable cost-effective long-duration discharge.[4−9]

The all-vanadium redox flow battery chemistry is currently the most technologically developed but may not access much of the grid storage market due to electrolyte cost constraints.[6,9−13] Emerging organic electrolytes comprising cheaper earth-abundant elements may address this limitation.[14−39] However, organic electrolytes are more prone to molecular decomposition, which can lead to a progressive loss of charge storage capacity. Although several studies have proposed decomposition pathways, such as Michael addition,[19,22,31,40,41] nucleophilic substitution,[25,31,34] electrophilic aromatic substitution,[39] ring-opening,[17] and disproportionation,[25,33,37] none of these pathways have been linked quantitatively to capacity fade.

Here we identify irreversible dimerization as the mechanism of capacity loss in a RFB utilizing the inexpensive redox couples of 2,6-dihydroxyanthraquinone (DHAQ) and potassium salts of iron hexacyanide (Fe(CN)$_6$). We further demonstrate that capacity loss can be suppressed through simple modifications of the battery operating conditions.

Under ideal conditions, discharging a flow battery involves the reversible oxidation and concurrent reduction of the low potential (negolyte) and high potential (posolyte) active species, respectively. In a DHAQ/Fe(CN)$_6$ flow battery, the reactions and potentials vs SHE are[16]

$$\text{Negolyte: } DHAQ^{2-} + 2e^- \rightleftharpoons DHAHQ^{4-} \quad -680 \text{ mV; (pH 14)}$$

$$\text{Posolyte: } [Fe(CN)_6]^{3-} + e^- \rightleftharpoons [Fe(CN)_6]^{4-} \quad +510 \text{ mV}$$

In practice, decomposition of the negolyte active species causes the battery capacity to fade at ∼5−8%/day. As this rate limits the lifetime to the order of 1 week, identifying and inhibiting the mechanism of capacity loss is critical for the battery to approach the decadal service life that will be necessary for large-scale grid storage applications.[42]

■ RESULTS AND DISCUSSION

To identify the chemical origin of negolyte active species degradation,[43] we cycled a sample of DHAQ electrolyte repeatedly over the course of several days in a symmetric cell and analyzed its composition (Figure S1). In addition to deprotonated forms of DHAQ and its intended reduction product, dihydroxyanthrahydroquinone (DHAHQ), we identified the decomposition products 2,6-dihydroxyanthrone (DHA) and its dimers ((DHA)$_2$) (see Scheme 1).

The identification of DHA was enabled by precisely controlling cycling conditions (Figure S2). The structure of DHA was suggested by high resolution mass spectrometry and

Scheme 1. Intended Operation and Decomposition Pathway of a DHAQ/Fe(CN)$_6$ Flow Battery^a
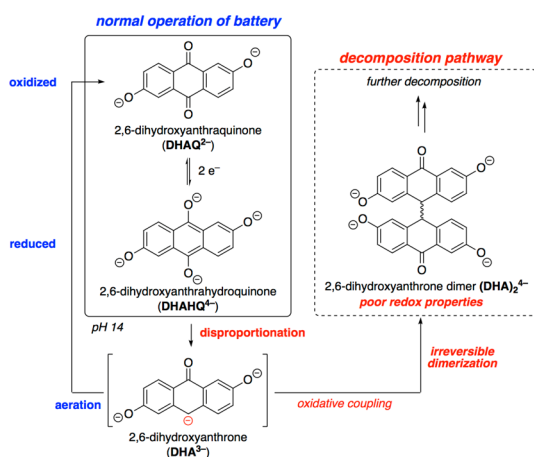
^{a}DHA is depicted in its presumed protonation state at pH 14 as DHA^{3-}.

confirmed by an exact match to the ^{1}H NMR spectrum and HPLC retention time of an authentic sample (Figures S3–S5). When samples containing DHA were subjected to electrochemical oxidation (Figure S6), mass spectrometric peaks corresponding to (DHA)$_2$ were observed (Figure S7). The assignment of (DHA)$_2$ was confirmed by the isolation of pure samples by preparative HPLC and subsequent NMR analysis (Figures S8 and S9).

Beck and Heydecke observed anthrone formation during electrochemical reduction of unsubstituted anthraquinone under highly acidic conditions and proposed homogeneous disproportionation as the mechanism by which this transformation occurs.[44] Two observations suggest that DHAHQ in alkaline solution undergoes disproportionation as well. First, increasing the reduction overpotential beyond the potential required to reduce DHAQ to DHAHQ does not increase the rate of capacity loss.[43] Additionally, increasing proportions of DHA are formed when DHAHQ is held away from the electrodes in a sealed vial for increasing durations (Figure S10). This disproportionation would occur according to the following proposed reaction:

$$2DHAHQ^{4-} + 2H_2O \rightarrow DHAQ^{2-} + DHA^{3-} + 3OH^-$$

Under the highly alkaline conditions within the negolyte compartment (Figure S11), facile one-electron oxidation of the DHA carbanion, followed by radical dimerization, would lead to (DHA)$_2$. Indeed, pure samples of DHA are completely and irreversibly converted to (DHA)$_2$ when subjected to electrochemical oxidation under alkaline and anaerobic conditions (Figure S12). However, under aerobic conditions, oxidation of DHA back to DHAQ can be favored over dimerization (Figures 1A and S13), particularly at low DHA concentration (Figures S14 and S15). Precedents for the oxidation of anthrone species to anthraquinone and dianthrone species may be found in refs 45–56.

The irreversible conversion of DHAHQ to (DHA)$_2$ has a deleterious effect on battery operation due to the replacement of the anthraquinone moiety with a benzophenone functional group (Figures 1B and S16A). Although (DHA)$_2$ is also redox-active, its use in a RFB is impractical for several reasons. First, the higher reduction potential of (DHA)$_2$ with respect to
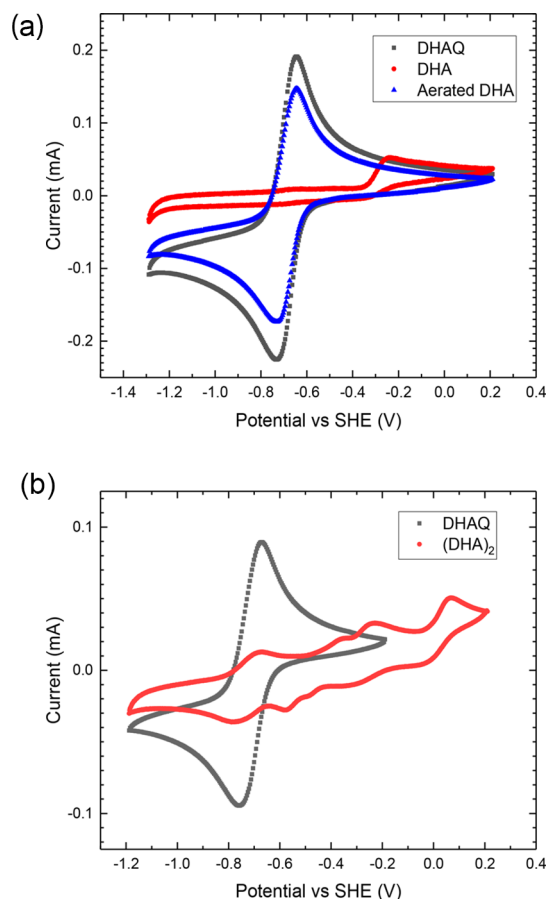

Figure 1. (A) Cyclic voltammetry of 10 mM synthesized DHA at pH 14 under a nitrogen atmosphere. After aeration, redox activity is recovered through conversion of DHA to DHAQ. A separate 10 mM DHAQ sample is shown for comparison. (B) (DHA)$_2$ has a higher redox potential than DHAQ, which leads to poor battery performance. Cyclic voltammograms were obtained separately for DHAQ and (DHA)$_2$, both at 5 mM in 1 M KOH. The (DHA)$_2$ sample contained a ∼5% DHAQ impurity.

DHAQ (Figure 1B) decreases the overall potential of the battery prohibitively.[11] Second, even with strong overpotentials, cycling accesses only two electrons per molecule (Figure S16B). Thus, at twice the molecular weight of DHAQ, (DHA)$_2$ has half the capacity by mass. Finally, (DHA)$_2$ is unstable at pH 14 (Figure S17). These findings indicate that the conversion of DHAQ to (DHA)$_2$ engenders a progressive loss of battery capacity.

To establish that irreversible dimerization is the primary mechanism of capacity loss, we quantitatively correlated the decrease in concentrations of DHAQ and DHAHQ with the extent of capacity loss. We subjected a typical flow battery containing 0.1 M DHAQ/DHAHQ to symmetric cell-cycling at pH 14 (8 cycles over ∼5 h). When cycling was stopped and the capacity-limiting side held in a reduced state for 43 h, the battery capacity decreased by 15% (Figure 2) when corrected for aliquot volume removal. When cycling with ±350 mV discharge overpotential was resumed, the first oxidative discharge half-cycle included the transient capacity associated with the irreversible conversion of DHA to (DHA)$_2$. ^{1}H NMR analysis of an aliquot of negolyte removed after aging revealed that the total concentration of DHAQ had declined by 16%. This decrease was mass-balanced by an increase in DHA
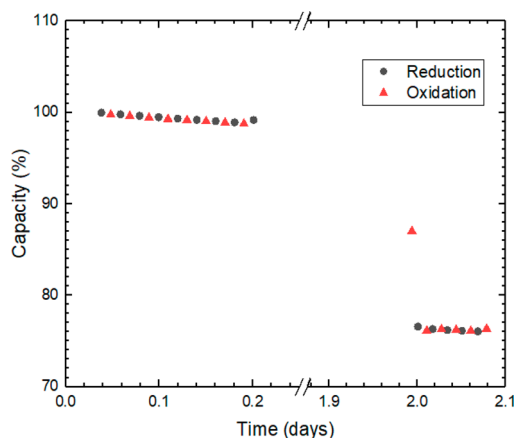
Figure 2. Pausing redox cycling in the reduced state adversely affects battery capacity. Symmetric-cell cycling (see SI) for 8 cycles, followed by a 43 h pause, leads to a large drop in capacity. The first oxidative discharge after the pause shows a transient amount of capacity corresponding to the conversion of accumulated DHA to $(DHA)_2$.

concentration of 16% (as determined by NMR analysis). Both quantities correspond well to the observed loss in capacity of 15%. In addition, all of the DHA formed was measurably converted to $(DHA)_2$ (Figures S18−S20). These observations strongly implicate anthrone formation and subsequent dimerization as the primary source of capacity loss. Anthrone and dianthrone species have also been reported to be products of the chemical reduction of anthraquinones and of the electrochemical reduction of anthraquinones in acidic aqueous solutions.[44,57−65]

The finding that irreversible dimerization is linked to the redox chemistry of anthraquinones may limit the ongoing search for quinones with lower potentials. This is because any decrease in the reduction potential of the quinone/hydroquinone couple may simultaneously increase the propensity for the hydroquinone to disproportionate into anthrone and quinone. This hypothesis is supported both by calculations (Figure 3; PM7/COSMO on a subset of molecules from ref 41) and the experimental properties of 4,4′-((9,10-anthraquinone-2,6-diyl)dioxy)dibutyrate (2,6-DBEAQ).[34] This negolyte active species has a reduction potential that is 180 mV higher
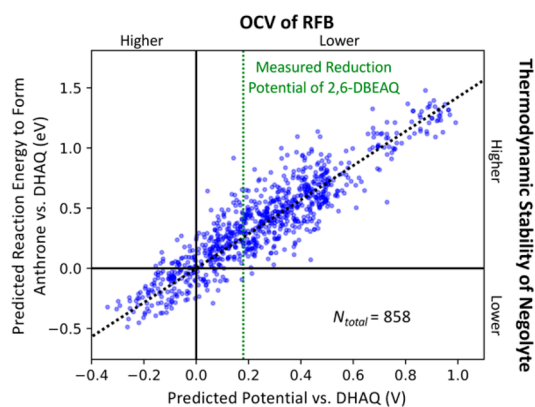

Figure 3. Trade-off between the reduction potential of the quinone-hydroquinone couple and the thermodynamic stability of the hydroquinone form toward anthrone formation (N_{total} = 858 quinones). The mean absolute errors (previously benchmarked in ref 41) of the predicted DHAQ potentials is ~0.07 V.

than that of DHAQ and is approximately 100 times more stable in terms of RFB lifetime.[34] In addition to the associated decrease in battery voltage that this higher reduction potential entails, 2,6-DBEAQ is synthesized from DHAQ, increasing its cost.[34] Strategies that can increase the lifetime of anthraquinones independently of their redox potential would therefore be valuable.

Two simple changes to the operating conditions of the battery may be used to greatly decrease the rate of capacity loss. Because the degradation pathway is initiated by disproportionation of DHAHQ, we hypothesized that avoiding high states of charge would decrease the amount of DHA formed (Figure S21), thereby extending battery life. When a DHAQ/Fe(CN)$_6$ flow battery was cycled at 100 mA/cm^2 with a 1.25 V cutoff that accessed 88% of the theoretical capacity, the observed capacity declined at only 0.14%/day (Figures 4A and S22A). By contrast, under more typical conditions with a 1.6 V cutoff that accessed 99.9% of the theoretical capacity, the observed capacity declined at 5.6%/day. Similar results were obtained by using identical potential conditions but with a Coulombic cutoff to restrict the SOC range (Figure S23).
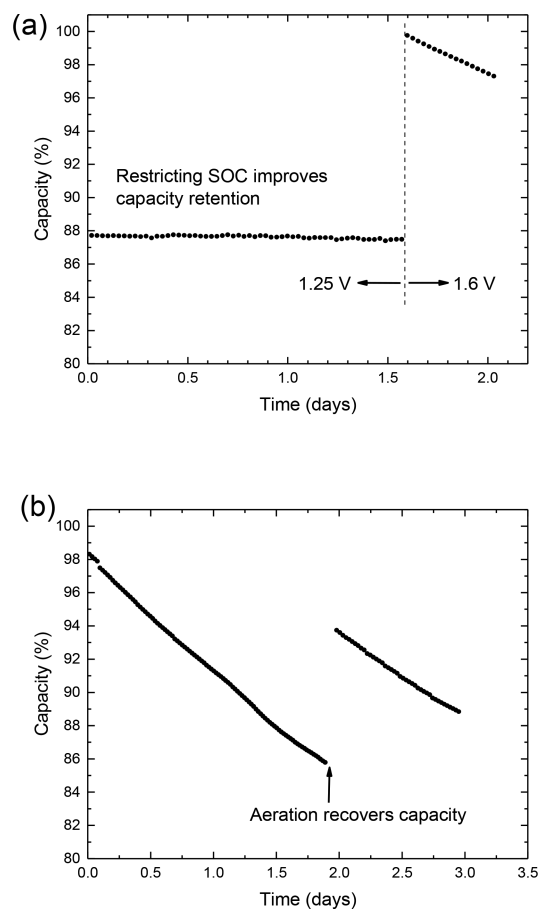

Figure 4. (A) Limiting the state of charge reduces the rate of capacity loss in a negolyte-limited DHAQ/Fe(CN)$_6$ full cell. Over the first 1.6 days, the operating state of charge was limited to 88% of the theoretical capacity (i.e., 88% DHAHQ and 12% DHAQ), and the capacity faded at only 0.14%/day. The right-hand segment reflects typical operating conditions (cycling to 99.9% of theoretical capacity), and the capacity faded at 5.6%/day. (B) Symmetric cell cycling in which the capacity-limiting side (5 mL of 0.1 M DHAQ in 1.2 M KOH) demonstrates recovery of 70% of lost capacity after aeration of discharged electrolyte.

These observations demonstrate that operating conditions that access most, but not all, of the theoretical capacity greatly extend battery lifetime.

Although the strategy of avoiding high states of charge reduces the amount of DHA formation, it does not eliminate it completely unless impractically low (less than ~60%) states of charge are utilized (Figure S21). To divert the remaining DHA from irreversible dimerization and prevent the associated loss of capacity, we used lower oxidation overpotentials to slow the rate of DHA dimerization. We then added molecular oxygen to favor the oxidation of DHA back to DHAQ over DHA dimerization (Scheme 1). We tested this strategy by symmetric cell cycling of a DHAQ electrolyte under anaerobic conditions within its full SOC range (0−99.9%) but with an oxidative overpotential of 200 mV. The capacity decreased by 13% (Figures 4B and S22B) over 2 days of cycling. At this point, the electrolyte was removed from the glovebox in the discharged (oxidized) state, aerated, and returned to service. This operation resulted in the recovery of approximately 70% of the lost capacity when cycling was resumed. In a large-scale flow battery, the same process might be made more effective by purging the DHAQ negolyte reservoir with air after each full discharge to exploit the high DHAQ recovery rate at low DHA concentrations. Aeration could be optimized to match the DHA concentration to avoid unnecessary current efficiency loss (Figure S24).

Our findings establish that the progressive loss of capacity in a DHAQ-based flow battery is primarily due to anthrahydroquinone disproportionation followed by irreversible anthrone dimerization. Computational analysis indicates that the propensity for anthrahydroquinones to disproportionate is highly correlated to the redox potential of the anthraquinone. Therefore, the use of anthraquinones with lower reduction potentials, enabling apparently higher cell voltages, may be limited by a decrease in stability. This correlation suggests that ongoing efforts to improve quinone-based negolytes might profitably be redirected toward the manipulation of properties such as their solubility and synthetic costs, rather than redox potential alone.

We have also shown that the loss of battery capacity can largely be ameliorated by avoiding high states of charge and by negolyte aeration. We estimate that the combination of these two strategies would reduce the capacity fade rate of anthraquinone-based flow batteries by approximately 2 orders of magnitude, from 5.6%/day to $(0.3)(0.14\%/\text{day}) = 0.042\%/$day. These modified operating procedures should not substantially increase the estimated large-scale capital cost (~$20/kWh for the DHAQ negolyte).[66] By comparison, the United States Department of Energy has set a $150/kWh goal for grid-based energy storage systems. With further optimization of the battery operating conditions, this goal may be attained in the near future.

ASSOCIATED CONTENT

Ⓢ Supporting Information

The Supporting Information is available free of charge on the ACS Publications website at DOI: 10.1021/jacs.8b13295.

Experimental details (PDF)

AUTHOR INFORMATION

Corresponding Authors

*gordon@chemistry.harvard.edu

*maziz@harvard.edu

*ekwan@fas.harvard.edu

ORCID Ⓞ

Liuchuan Tong: 0000-0001-6211-6322

Daniel P. Tabor: 0000-0002-8680-6667

Susan A. Odom: 0000-0001-6708-5852

Alán Aspuru-Guzik: 0000-0002-8277-4434

Roy G. Gordon: 0000-0001-5980-268X

Michael J. Aziz: 0000-0001-9657-9456

Present Addresses

⊥Form Energy Inc., Somerville, Massachusetts 02143, United States

¶Department of Chemistry and Department of Computer Science; Vector Institute for Artificial Intelligence, University of Toronto, Toronto, Ontario M5S 1A1, Canada

Author Contributions

‖These authors contributed equally.

Notes

The authors declare the following competing financial interest(s): Harvard University has filed a patent application based on the methods described here.

REFERENCES

(1) Stehly, T.; Heimiller, D.; Scott, G. *2016 Cost of Wind Energy Review*; National Renewable Energy Laboratory, 2017.

(2) Dunn, B.; Kamath, H.; Tarascon, J. M. Electrical energy storage for the grid: a battery of choices. *Science* **2011**, *334* (6058), 928−35.

(3) Yang, Z.; Zhang, J.; Kintner-Meyer, M. C.; Lu, X.; Choi, D.; Lemmon, J. P.; Liu, J. Electrochemical energy storage for green grid. *Chem. Rev.* **2011**, *111* (5), 3577−613.

(4) Nguyen, T.; Savinell, R. F. Flow Batteries. *Electrochem. Soc. Interface* **2010**, *19*, 54−56.

(5) Rugolo, J.; Aziz, M. J. Electricity storage for intermittent renewable sources. *Energy Environ. Sci.* **2012**, *5*, 7151.

(6) Weber, A. Z.; Mench, M. M.; Meyers, J. P.; Ross, P. N.; Gostick, J. T.; Liu, Q. Redox flow batteries: a review. *J. Appl. Electrochem.* **2011**, *41* (10), 1137−1164.

(7) Leung, P.; Li, X.; Ponce de León, C.; Berlouis, L.; Low, C. T. J.; Walsh, F. C. Progress in redox flow batteries, remaining challenges and their applications in energy storage. *RSC Adv.* **2012**, *2* (27), 10125.

(8) Biello, D. Solar Wars. *Sci. Am.* **2014**, *311* (5), 66−71.

(9) Skyllas-Kazacos, M.; Chakrabarti, M. H.; Hajimolana, S. A.; Mjalli, F. S.; Saleem, M. Progress in Flow Battery Research and Development. *J. Electrochem. Soc.* **2011**, *158* (8), R55.

(10) Soloveichik, G. L. Flow batteries: current status and trends. *Chem. Rev.* **2015**, *115* (20), 11533−58.

(11) Darling, R. M.; Gallagher, K. G.; Kowalski, J. A.; Ha, S.; Brushett, F. R. Pathways to low-cost electrochemical energy storage: a

comparison of aqueous and nonaqueous flow batteries. *Energy Environ. Sci.* **2014**, 7 (11), 3459−3477.

(12) Winsberg, J.; Hagemann, T.; Janoschka, T.; Hager, M. D.; Schubert, U. S. Redox-Flow Batteries: From Metals to Organic Redox-Active Materials. *Angew. Chem. Int. Ed.* **2017**, 56 (3), 686−711.

(13) Huskinson, B.; Rugolo, J.; Mondal, S. K.; Aziz, M. J. A High Power Density, High Efficiency Hydrogen-Chlorine Regenerative Fuel Cell with a Low Precious Metal Content Catalyst. *Energy Environ. Sci.* **2012**, 5 (9), 8690.

(14) Huskinson, B.; Marshak, M. P.; Suh, C.; Er, S.; Gerhardt, M. R.; Galvin, C. J.; Chen, X.; Aspuru-Guzik, A.; Gordon, R. G.; Aziz, M. J. A metal-free organic-inorganic aqueous flow battery. *Nature* **2014**, 505 (7482), 195−8.

(15) Janoschka, T.; Martin, N.; Martin, U.; Friebe, C.; Morgenstern, S.; Hiller, H.; Hager, M. D.; Schubert, U. S. An aqueous, polymer-based redox-flow battery using non-corrosive, safe, and low-cost materials. *Nature* **2015**, 527, 78−81.

(16) Lin, K.; Chen, Q.; Gerhardt, M. R.; Tong, L.; Kim, S. B.; Eisenach, L.; Valle, A. W.; Hardee, D.; Gordon, R. G.; Aziz, M. J.; Marshak, M. P. Alkaline quinone flow battery. *Science* **2015**, 349 (6255), 1529.

(17) Lin, K.; Gómez-Bombarelli, R.; Beh, E. S.; Tong, L.; Chen, Q.; Valle, A.; Aspuru-Guzik, A.; Aziz, M. J.; Gordon, R. G. A redox-flow battery with an alloxazine-based organic electrolyte. *Nature Energy* **2016**, 1 (9), 16102.

(18) Orita, A.; Verde, M. G.; Sakai, M.; Meng, Y. S. A biomimetic redox flow battery based on flavin mononucleotide. *Nat. Commun.* **2016**, 7 (1), 13230.

(19) Hoober-Burkhardt, L.; Krishnamoorthy, S.; Yang, B.; Murali, A.; Nirmalchandar, A.; Surya Prakash, G. K.; Narayanan, S. R. A new Michael-reaction-resistant benzoquinone for aqueous organic redox flow batteries. *J. Electrochem. Soc.* **2017**, 164 (4), A600−A607.

(20) Liu, T.; Wei, X.; Nie, Z.; Sprenkle, V.; Wang, W. A Total Organic Aqueous Redox Flow Battery Employing a Low Cost and Sustainable Methyl Viologen Anolyte and 4-HO-TEMPO Catholyte. *Adv. Energy Mater.* **2016**, 6 (3), 1501449.

(21) Yang, B.; Hoober-Burkhardt, L.; Wang, F.; Surya Prakash, G. K.; Narayanan, S. R. An inexpensive aqueous flow battery for large-scale electrical energy storage based on water-soluble organic redox couples. *J. Electrochem. Soc.* **2014**, 161, A1371−A1380.

(22) Yang, B.; Hoober-Burkhardt, L.; Krishnamoorthy, S.; Murali, A.; Surya Prakash, G. K.; Narayanan, S. R. High-Performance Aqueous Organic Flow Battery with Quinone-Based Redox Couples at Both Electrodes. *J. Electrochem. Soc.* **2016**, 163, A1442−A1449.

(23) Janoschka, T.; Martin, N.; Hager, M. D.; Schubert, U. S. An Aqueous Redox-Flow Battery with High Capacity and Power: The TEMPTMA/MV System. *Angew. Chem. Int. Ed.* **2016**, 55, 14427−14430.

(24) Hu, B.; DeBruler, C.; Rhodes, Z.; Liu, T. L. Long-Cycling Aqueous Organic Redox Flow Battery (AORFB) toward Sustainable and Safe Energy Storage. *J. Am. Chem. Soc.* **2017**, 139 (3), 1207−1214.

(25) Beh, E. S.; De Porcellinis, D.; Gracia, R. L.; Xia, K. T.; Gordon, R. G.; Aziz, M. J. A neutral pH aqueous organic−organometallic redox flow battery with extremely high capacity retention. *ACS Energy Lett.* **2017**, 2 (3), 639−644.

(26) DeBruler, C.; Hu, B.; Moss, J.; Liu, X.; Luo, J.; Sun, Y.; Liu, T. L. Designer two-electron storage viologen anolyte materials for neutral aqueous organic redox flow batteries. *Chem.* **2017**, 3, 961−978.

(27) Janoschka, T.; Morgenstern, S.; Hiller, H.; Friebe, C.; Wolkersdorfer, K.; Haupler, B.; Hager, M. D.; Schubert, U. S. Synthesis and characterization of TEMPO- and viologen- polymers for water-based redox-flow batteries. *Polym. Chem.* **2015**, 6 (45), 7801−7811.

(28) Winsberg, J.; Stolze, C.; Muench, S.; Liedl, F.; Hager, M. D.; Schubert, U. S. TEMPO/phenazine combi-molecule: a redox-active material for symmetric aqueous redox-flow batteries. *ACS Energy Lett.* **2016**, 1 (5), 976−980.

(29) Hollas, A.; Wei, X.; Murugesan, V.; Nie, Z.; Li, B.; Reed, D.; Liu, J.; Sprenkle, V.; Wang, W. A biomimetic high-capacity phenazine-based anolyte for aqueous organic redox flow batteries. *Nature Energy* **2018**, 3 (6), 508−514.

(30) Li, Z.; Li, S.; Liu, S.; Huang, K.; Fang, D.; Wang, F.; Peng, S. Electrochemical Properties of an All-Organic Redox Flow Battery Using 2,2,6,6-Tetramethyl-1-Piperidinyloxy and N-Methylphthalimide. *Electrochem. Solid-State Lett.* **2011**, 14 (12), A171.

(31) Wedege, K.; Drazevic, E.; Konya, D.; Bentien, A. Organic Redox Species in Aqueous Flow Batteries: Redox Potentials, Chemical Stability and Solubility. *Sci. Rep.* **2016**, 6, 39101.

(32) Xu, Y.; Wen, Y. H.; Cheng, J.; Cao, G. P.; Yang, Y. S. A study of tiron in aqueous solutions for redox flow battery application. *Electrochim. Acta* **2010**, 55 (3), 715−720.

(33) Orita, A.; Verde, M. G.; Sakai, M.; Meng, Y. S. The impact of pH on side reactions for aqueous redox flow batteries based on nitroxyl radical compounds. *J. Power Sources* **2016**, 321, 126−134.

(34) Kwabi, D. G.; Lin, K.; Ji, Y.; Kerr, E. F.; Goulet, M.-A.; De Porcellinis, D.; Tabor, D. P.; Pollack, D. A.; Aspuru-Guzik, A.; Gordon, R. G.; Aziz, M. J. Alkaline quinone flow battery with long lifetime at pH 12. *Joule* **2018**, 2, 1907.

(35) Luo, J.; Hu, B.; DeBruler, C.; Liu, T. A "π-Conjugation Extended Viologen" as Novel Two-Electron Storage Anolyte for Total Organic Aqueous Redox Flow Battery. *Angew. Chem. Int. Ed.* **2018**, 57 (1), 231−235.

(36) DeBruler, C.; Hu, B.; Moss, J.; Luo, J.; Liu, T. L. A sulfonate-functionalized viologen enabling neutral cation exchange, aqueous organic redox flow batteries toward renewable energy storage. *ACS Energy Lett.* **2018**, 3 (3), 663−668.

(37) Hu, B.; Tang, Y.; Luo, J.; Grove, G.; Guo, Y.; Liu, T. Improved Radical Stability of Viologen Anolyte in Aqueous Organic Redox Flow Battery. *Chem. Commun.* **2018**, 54, 6871.

(38) Hu, B.; Liu, T. L. Two electron utilization of methyl viologen anolyte in nonaqueous organic redox flow battery. *J. Energy Chem.* **2018**, 27 (5), 1326−1332.

(39) Murali, A.; Nirmalchandar, A.; Krishnamoorthy, S.; Hoober-Burkhardt, L.; Yang, B.; Soloveichik, G. L.; Surya Prakash, G. K.; Narayanan, S. R. Understanding and mitigating capacity fade in aqueous organic redox flow batteries. *J. Electrochem. Soc.* **2018**, 165 (7), A1193.

(40) Xu, Y.; Wen, Y. H.; Cheng, J.; Cao, G. P.; Yang, Y. S. Electrochemical Reaction Mechanism of Tiron in Acidic Aqueous Solution. *Adv. Mater. Res.* **2011**, 396−398, 1730−1735.

(41) Tabor, D. P.; Gómez-Bombarelli, R.; Tong, L.; Gordon, R. G.; Aziz, M. J.; Aspuru-Guzik, A. Theoretical and Experimental Investigation of the Stability Limits of Quinones in Aqueous Media: Implications for Organic Aqueous Redox Flow Batteries. *ChemRxiv* **2018**, DOI: 10.26434/chemrxiv.6990053.v2.

(42) Perry, M. L.; Weber, A. Z. Advanced Redox-Flow Batteries: A Perspective. *J. Electrochem. Soc.* **2016**, 163 (1), A5064−A5067.

(43) Goulet, M.-A.; Aziz, M. J. Flow Battery Molecular Reactant Stability Determined by Symmetric Cell Cycling Methods. *J. Electrochem. Soc.* **2018**, 165 (7), A1466−A1477.

(44) Beck, F.; Heydecke, G. On the Mechanism of the Cathodic Reduction of Anthraquinone to Anthrone. *Berichte der Bunsengesellschaft für physikalische Chemie* **1987**, 91 (1), 37−43.

(45) Serdyuk, A. A.; Kasianchuk, M. G.; Opeida, I. A. Kinetics of Amine Catalysed Oxidation of Anthrone by Oxygen in Aprotic Solvents. *Russ. J. Phys. Chem. A* **2010**, 84 (3), 391−394.

(46) Iwata, M.; Kuzuhara, H. Oxidation of Anthracenols and Anthrone to Anthraquinones with Oxygen Mediated by Copper(II) Ion and Imidazole. *Bull. Chem. Soc. Jpn.* **1985**, 58, 1609−1610.

(47) Cavey, D.; Caron, J.-C.; Shroot, B. Anthralin: Chemical instability and glucose-6-phosphate dehydrogenase inhibition. *J. Pharm. Sci.* **1982**, 71 (9), 980−983.

(48) Müller, K.; Eibler, E.; Mayer, K. K.; Wiegrebe, W.; Klug, G. Dithranol, Singlet Oxygen and Unsaturated Fatty Acids. *Arch. Pharm.* **1986**, 319, 2−9.

(49) Segal, A.; Katz, C.; Van Duuren, B. L. Structure and tumor-promoting activity of anthralin (1, 8-dihydroxy-9-anthrone) and related compounds. *J. Med. Chem.* **1971**, *14* (12), 1152−1154.

(50) Martinmaa, J.; Vanhala, L.; Mustakallio, K. K. Free radical intermediates produced by autoxidation of 1,8-dihydroxy-9-anthrone (dithranol) in pyridine. *Experientia* **1978**, *34*, 872−873.

(51) Davies, A. G.; Hawari, J. A.-A.; Whitefield, M. Generation and E.S.R. spectrum of the 1,8-dihydroxy-9-Anthron-10-yl radical. *Tetrahedron Lett.* **1983**, *24* (41), 4465−4468.

(52) Geiger, W. 1,8-Dihydroxyanthrone and two isomeric 1,1',8,8'-Tetrahydroxy-10,10'-bianthrones. *Chem. Ber.* **1974**, *107* (9), 2976−2984.

(53) Dabestani, R.; Hall, R. D.; Sik, R. H.; Chignell, C. F. Spectroscopic studies of cutaneous photosensitizing agents—XV. anthralin and its oxidation product 1,8-dihydroxyanthraquinone. *Photochem. Photobiol.* **1990**, *52* (5), 961−971.

(54) Majeski, E. J.; Stuart, J. D.; Ohnesorge, W. E. Controlled Potential Oxidation of Anthracene in Acetonitrile. *J. Am. Chem. Soc.* **1968**, *90* (3), 633−636.

(55) Fujii, I.; Chen, Z.-G.; Ebizuka, Y.; Sankawa, U. Identification of emodinanthrone oxygenase in fungus Aspergillus terreus. *Biochem. Int.* **1991**, *25* (6), 1043−1049.

(56) Chung, J.-y.; Fujii, I.; Harada, S.; Sankawa, U.; Ebizuka, Y. Expression, Purification, and Characterization of AknX Anthrone Oxygenase, Which Is Involved in Aklavinone Biosynthesis in Streptomyces galilaeus. *J. Bacteriol.* **2002**, *184* (22), 6115−6122.

(57) Wendlandt, A. E.; Stahl, S. S. Quinones in Hydrogen Peroxide Synthesis and Catalytic Aerobic Oxidation Reactions. In *Liquid Phase Aerobic Oxidation Catalysis: Industrial Applications and Academic Perspectives*, 1st ed.; Stahl, S. S., Alsters, P. L., Eds.; Wiley-VCH Verlag GmbH & Co. KGaA: Weinheim, Germany, 2016; pp 221−237.

(58) Perkin, A. G.; Whattam, T. W. XXXVI.—Some products of the reduction of 2-hydroxyanthraquinone. *J. Chem. Soc., Trans.* **1922**, *121*, 289−300.

(59) Goodall, F. L.; Perkin, A. G. LVIII.—Reduction products of the hydroxyanthraquinones. Part V. *J. Chem. Soc., Trans.* **1924**, *125*, 470−476.

(60) Comninellis, C.; Plattner, E. The electrochemical reduction of anthraquinone to anthrone in concentrated H2SO4. *J. Appl. Electrochem.* **1985**, *15* (5), 771−773.

(61) Shi, Z.-W.; Li, Y.-Z.; Li, Y.; Lu, G.-Y.; Liu, S.-H. 1,1′,8,8′-Tetramethoxy-10,10′-bianthrone. *Acta Crystallogr., Sect. E: Struct. Rep. Online* **2004**, *E60* (12), o2275−o2277.

(62) Shyamasundar, N.; Caluwe, P. Lithium aluminum hydride reduction of peri-alkoxy-9,10 anthraquinones. *J. Org. Chem.* **1981**, *46* (8), 1552−1557.

(63) Prinz, H.; Wiegrebe, W.; Müller, K. Syntheses of anthracenones. 1. Sodium dithionite reduction of *peri*-substituted anthracenediones. *J. Org. Chem.* **1996**, *61*, 2853−2856.

(64) Prinz, H.; Burgemeister, T.; Wiegrebe, W.; Müller, K. Syntheses of Anthracenones. 2. Preparation of 1,8-Dimethoxy- (Dimethylanthralin) and 4,5-Dihydroxy-9(10H)-anthracenone (Isoanthralin): A Revision. *J. Org. Chem.* **1996**, *61* (8), 2857−2860.

(65) Müller, K.; Leukel, P.; Ziereis, K.; Gawlik, I. Antipsoriatic Anthrones with Modulated Redox Properties. 2. Novel Derivatives of Chrysarobin and Isochrysarobin—Antiproliferative Activity and 5-Lipoxygenase Inhibition. *J. Med. Chem.* **1994**, *37* (11), 1660−1669.

(66) Yang, Z.; Tong, L.; Tabor, D. P.; Beh, E. S.; Goulet, M.-A.; De Porcellinis, D.; Aspuru-Guzik, A.; Gordon, R. G.; Aziz, M. J. Alkaline benzoquinone aqueous flow battery for large-scale storage of electrical energy. *Adv. Energy Mater.* **2018**, *8* (8), 1702056.

Correction to "Extending the Lifetime of Organic Flow Batteries via Redox State Management"

Marc-Antoni Goulet, Liuchuan Tong, Daniel A. Pollack, Daniel P. Tabor, Susan A. Odom, Alán Aspuru-Guzik, Eugene E. Kwan,* Roy G. Gordon,* and Michael J. Aziz*

Cite This: https://doi.org/10.1021/jacs.1c05529   Read Online

ACCESS | 📊 Metrics & More | 📖 Article Recommendations |

The additional data presented herein is intended to revisit a previous claim based upon Figure 4 of the original publication. More extensive trials now expose a clear trend between the restriction of negolyte state of charge (SOC) and the capacity fade rate of the DHAQ/Fe(CN)$_6$ flow battery. The authors now consider the fade rate of 0.14%/day claimed in the main text to be an outlier, as depicted by the red cross in Figure 1 below, and the data in Figure S23 of the original Supporting Information to be more representative of the achievable fade rate with an 88% SOC restriction. Upon further investigation, it was determined that cell cycling history is the most likely source of the discrepancy. The cell and electrolyte used in the experiment shown in Figure 4 of the original publication had undergone prior cycling, thereby accumulating the DHA decomposition product and slowing the rate of further decomposition; in contrast, the data for Figure S23 come from a pristine cell and electrolyte. This consideration was overlooked in the original analysis and can be an important direction for future study.

The overall conclusions of the original study remain unchanged. The present data affect only the degree to which the SOC restriction strategy minimizes the formation of the anthrone decomposition product of the fresh DHAQ negolyte. More specifically, the data herein indicate that a 10-fold (from 4.5 to 0.49%/day at 80% SOC restriction) or 15-fold (from 4.5 to 0.29%/day at 50% SOC restriction) decrease in capacity loss rate can be reproducibly achieved through SOC restriction alone, but not a 40-fold decrease (from 5.6 to 0.14%/day), as originally published. In addition, the aggregate data in Figure 1, collected under various conditions over an entire year, indicate the robustness of the trend to seasonal variability (~5 °C). Although most of the data in Figure 1 were obtained with a Coulombic capacity cutoff as in Figure S23, a few of the cell runs at 50% and 80% SOC restriction were obtained with a potential-controlled SOC cutoff similar to that used in Figure 4 of the original publication. Within error, these different cutoff conditions produce indistinguishable results, thereby showing that the type of cutoff condition is not the cause of the original discrepancy. In addition, the aggregate data contain cell runs at two different electrolyte concentrations, which suggests that the lifetime extension strategy is applicable to practical battery concentrations.
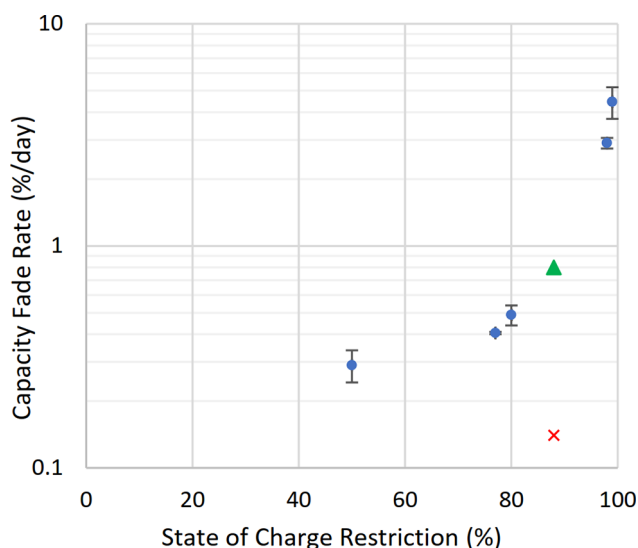

Figure 1. Aggregate cycling data from pristine cells and electrolytes elucidating a trend in capacity fade rate as a function of DHAQ negolyte SOC restriction. All data were obtained by comparing capacity immediately before and after SOC-restricted segments. All cells were cycled galvanostatically with potential holds and composed of one of two possible electrolyte formulations consisting of either 0.1 M DHAQ in 1.2 M KOH as negolyte vs 0.07 M K$_4$[Fe(CN)$_6$] and 0.01 M K$_3$[Fe(CN)$_6$] in 1 M KOH as posolyte, or 0.5 M DHAQ in 2 M KOH as negolyte vs 0.35 M K$_4$[Fe(CN)$_6$] and 0.05 M K$_3$[Fe(CN)$_6$] in 1 M KOH as posolyte, where the posolytes generally have 6× the volume and therefore >2× the capacity of the negolytes. The green triangle data point at 88% SOC restriction is from Figure S23 in the Supporting Information of the original publication, whereas the red cross represents the result from Figure 4 of the original main text. Data points at 50%, 80%, 98%, and 99% SOC restriction each consist of at least five cell runs.

■ ACKNOWLEDGMENTS

Supporting Information

Extending the Lifetime of Organic Flow Batteries via Redox State Management

Marc-Antoni Goulet,[†,‖,⊥] Liuchuan Tong,[‡,‖] Daniel A. Pollack,[§] Daniel P. Tabor,[‡] Susan A. Odom,[†,∇] Alán Aspuru-Guzik,[‡,¶] Eugene E. Kwan,[*,‡] Roy G. Gordon,[*,†,‡] and Michael J. Aziz[*,†]

[†]Harvard John A. Paulson School of Engineering and Applied Sciences, Harvard University, Cambridge, Massachusetts 02138, United States

[‡]Department of Chemistry and Chemical Biology, Harvard University, Cambridge, Massachusetts 02138, United States

[§]Department of Physics, Harvard University, Cambridge, Massachusetts 02138, United States

[∇]Department of Chemistry, University of Kentucky, Lexington, Kentucky 40506, United States

[‖]These authors contributed equally.

Present Addresses

[⊥] Form Energy, Inc., Somerville, Massachusetts 02143, United States

[¶] Department of Chemistry and Department of Computer Science; Vector Institute for Artificial Intelligence, University of Toronto, Toronto, Ontario M5S 1A1, Canada

Table of Contents

Experimental methods

Cell cycling

All flow cell cycling tests were performed with a 5 cm^2 cell (Fuel Cell Tech, Albuquerque, NM) equipped with POCO sealed graphite flow plates with serpentine flow fields. Each side of the cell contained a stack of four sheets of Sigracet SGL 39AA porous carbon paper that had been pretreated by baking in air at 400 °C for 24 h. In all cases, the cell was assembled with a Nafion N117 membrane that had been pretreated by immersion in a 1 M KOH aqueous solution for at least 72 hours. In all cases, Viton (PVDF) gaskets were used to seal the electrodes between the membranes and graphite flow fields. Flow of electrolytes was forced with a Cole-Parmer Masterflex L/S peristaltic pump, which required a small length of Viton peristaltic tubing. All other tubing and electrolyte reservoirs were made from chemically resistant fluorinated ethylene propylene (FEP).

Potentiostatic cycling of all volumetrically-unbalanced compositionally-symmetric cells was performed in a glovebox with < 2 ppm of oxygen with a Biologic VSP 300 potentiostat. Unless otherwise specified, the potential limits were set to ±200 mV to access > 99% of the available DHAQ capacity. As explained below, the oxidation potential was increased to +350 mV in some cases in order to oxidize any DHA present in the electrolyte. Due to the starting 50% SOC, these potential limits can be considered similar to overpotentials being divided for each side of the cell. In all symmetric cells, the non-capacity-limiting side comprised twice the volume of 50% SOC electrolyte as the capacity-limiting side. For example, if the capacity-limiting side contained 5 mL of 50% SOC 0.1 M DHAQ/DHAHQ and 1.2 M KOH, then the non-capacity-limiting side contained 10 mL of the same electrolyte. Due to these unbalanced volumes, the overpotentials are not split exactly evenly between the capacity-limiting and non-capacity-limiting sides of the cell.

Electrolyte preparation

Unless otherwise specified, DHAQ electrolytes were prepared as aqueous solutions at 0.1 M concentration with 1.2 M KOH in order to deprotonate the DHAQ and afford a pH 14 solution. For symmetric cell testing, this electrolyte was charged in a full cell against potassium ferrocyanide until the current decayed to a steady state value less than 1 mA cm^{-2} and was then mixed in equal proportions with uncharged material in order to make a 50% SOC electrolyte.

^{1}H NMR spectroscopy

Unless otherwise specified, NMR analysis of cycled electrolytes was performed by diluting 80 μL of the DHAQ electrolyte in 720 μL of D$_2$O containing approximately 10 mM of sodium

methanesulfonate (δ 2.6 ppm) as an internal standard. Spectra were recorded on a Varian INOVA 500 MHz spectrometer unless otherwise specified.

General information for synthesis

^{1}H NMR and ^{13}C NMR spectra were recorded on Varian INOVA 500 spectrometers unless otherwise specified. NMR spectra were recorded in solutions of deuterated dimethyl sulfoxide (DMSO-d_6) with the residual dimethyl sulfoxide (δ 2.49 ppm for ^{1}H NMR and δ 39.5 ppm for ^{13}C NMR) taken as the internal reference and deuterated water (D$_2$O) with the residual water (δ 4.79 ppm for ^{1}H NMR) taken as the internal reference. All solvents and reagents were purchased from Sigma-Aldrich or Alfa Aesar and were used as received unless otherwise specified.

High resolution LC-MS

High-resolution LC-MS analysis was performed in the Small Molecule Mass Spectrometry Facility at Harvard University on a Bruker Impact II q-TOF with internal calibration sodium formate clusters. Liquid chromatography was performed on an Agilent 1290 Infinity HPLC using an Allure PFPP column (5 µm particle size, 150 x 2.1 mm) at a flow rate of 0.4 mL/min, and the following elution conditions were applied (solvent A = 0.1% v/v formic acid in water; solvent B = 0.1% v/v formic acid in acetonitrile): 95% solvent A for 2 min, a gradient increasing from 5% to 60% solvent B in solvent A over 13 min, a gradient increasing to 95% solvent B over 5 min, a gradient decreasing to 5% solvent B in solvent A over 0.1 min, and 95% solvent A for 4.9 min. The ESI mass spectra were recorded in negative ionization mode.

Preparative-scale HPLC

Liquid chromatography was performed using a Thermo Scientific Hypersil GOLD aQ column (5 µm particle size, 250 x 20 mm) at a flow rate of 10 mL/min, and the following elution conditions were applied (solvent A = 0.1% v/v formic acid in water; solvent B = 0.1% v/v formic acid in acetonitrile): 80% solvent A for 2 min, a gradient increasing from 20% to 70% solvent B in solvent A over 5 min, a gradient increasing to 85% solvent B over 10 min, a gradient increasing to 95% solvent B over 4 min, a gradient decreasing to 20% solvent B in solvent A over 1 min, and 80% solvent A for 2 min. The eluent fractions were collected and lyophilized for subsequent LC-MS confirmation.

Capacity fade of DHAQ symmetric cell

Fig. S1 depicts results of a volumetrically-unbalanced compositionally-symmetric cell cycling experiment performed potentiostatically with overpotentials of ±200 mV, accessing > 99% of the theoretical DHAQ capacity.[1] Cycling was continued for several days (363 cycles) in order to achieve significant capacity loss and perform post-mortem electrolyte analysis. A fade rate of approximately 8%/day was observed in this experiment.
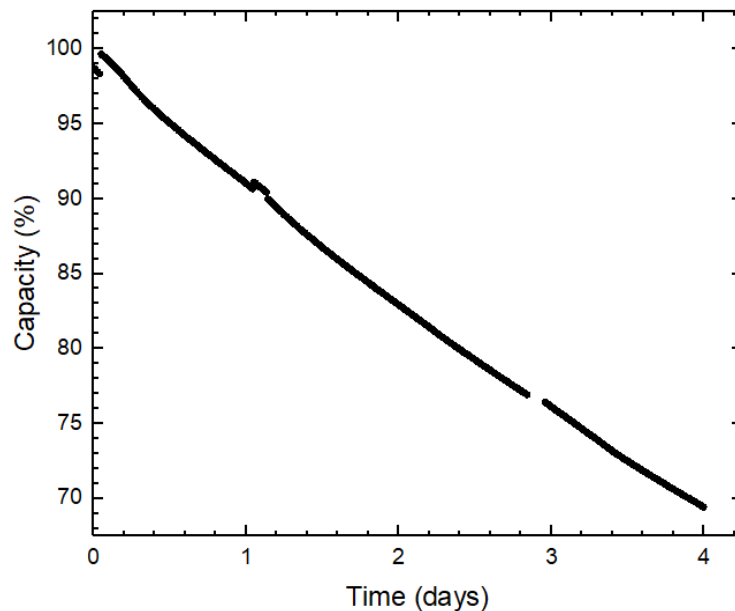

Figure S1. Unbalanced compositionally-symmetric cell cycling of 0.1 M DHAQ in a 1.2 M KOH solution, demonstrating loss of capacity over time.

Formation and detection of 2,6-dihydroxyanthrone (DHA)

Fig. S2a depicts results of a symmetric cell cycling experiment that began with a strong discharging (oxidation) overpotential of +350 mV, initially accessing > 99% of the theoretical DHAQ capacity. Near day 0.5 of cycling, the oxidation overpotential was lowered to +200 mV, leading to a sudden drop in capacity. Cycling was continued with this oxidative overpotential for several days, and aliquots were taken periodically in the discharged state for ^{1}H NMR spectroscopy. The presence and increasing intensity of new peaks in the NMR spectrum indicates the accumulation of another chemical species besides DHAQ.
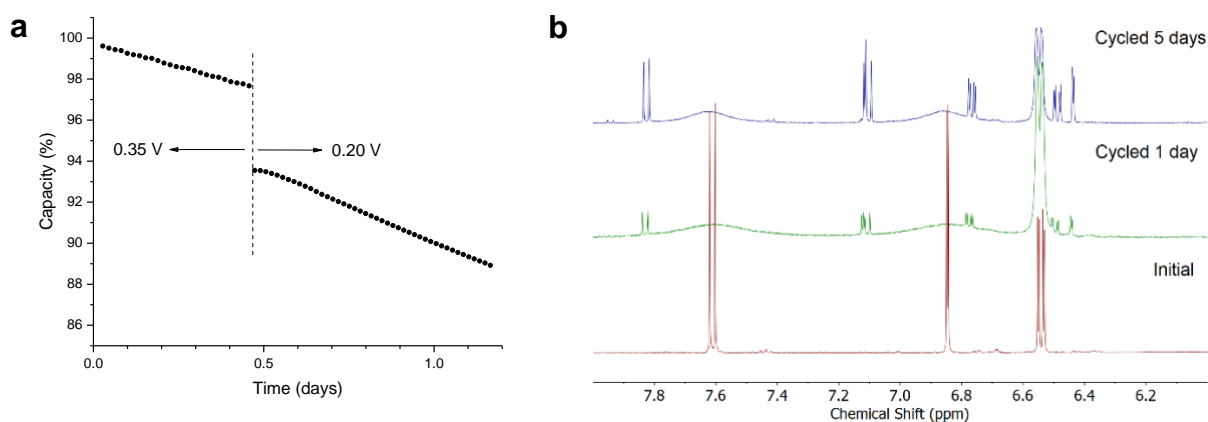
Figure S2. (a) Symmetric cell cycling of 0.1 M DHAQ in a 1.2 M KOH solution, showing change in capacity and fade rate when oxidation overpotential is changed from +350 to +200 mV. (b) Continued cycling at +200 mV oxidation overpotential leads to broadening of DHAQ peaks and to the appearance of additional peaks of increasing intensity in the ^{1}H NMR spectrum in D$_2$O. (Bottom spectrum is DHAQ, middle spectrum is electrolyte cycled for 1 day, top spectrum is electrolyte cycled for 5 days).

Identification of DHA

The capacity-limiting electrolyte utilized in the experiment of which results are depicted in Fig. S2 was collected after several days of further cycling with a +200 mV oxidation overpotential. Initial HPLC-MS analysis suggested primarily one major compound in addition to DHAQ, namely 2,6-dihydroxyanthrone (DHA). To verify the identification of DHA as the major side-product of DHAQ cell cycling at this potential, DHA was synthesized (Fig. S3) and confirmed to have the same retention time in HPLC-MS (Fig. S4). In addition, NMR spectroscopy was also performed on a mixture of synthesized DHA and DHAQ to simulate the cycled electrolyte. The NMR spectrum of DHA-spiked DHAQ (Fig. S5) qualitatively matches the spectrum of discharged cycled DHAQ (Fig. S2b).
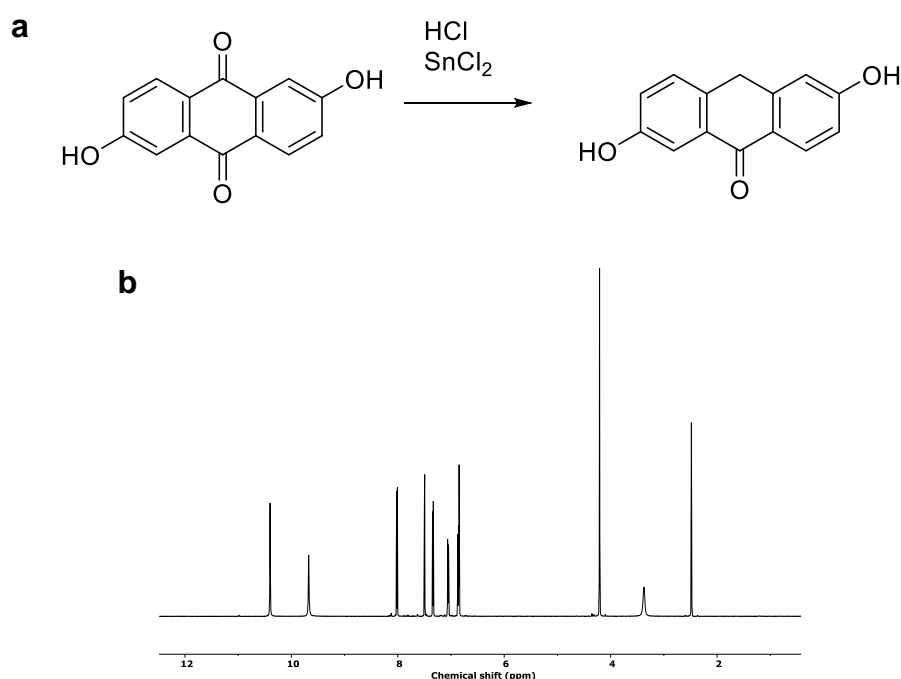
Figure S3. (a) Chemical synthesis of DHA. (b) ^{1}H NMR spectrum of synthetic DHA in DMSO-d_6.

2,6-Dihydroxyanthrone (DHA). The synthesis of DHA (Fig. S3a) was carried out according to a reported procedure[2] with modifications. 2,6-dihydroxyanthraquinone (DHAQ, 2.40 g, 10.0 mmol) and stannous chloride (15.2 g, 80.0 mmol) were refluxed for 7 h in 80 mL of concentrated hydrochloric acid. The resulting solution was cooled to room temperature, and the precipitate was collected by vacuum filtration. The collected solid was washed with DI water. The product was dried *in vacuo* to afford 2.20 g pale yellow powder (97% yield).

[1]**H NMR** (600 MHz, DMSO-d_6) δ 10.41 (s, 1H), 9.69 (s, 1H), 8.03 (d, J = 8 Hz, 1H), 7.51 (d, J = 3 Hz, 1H), 7.35 (d, J = 8 Hz, 1H), 7.06 (dd, J = 8 Hz, 3 Hz, 1H), 6.87 (m, 2H), 4.22 (s, 2H) **HRMS** (ESI) m/z: calcd for $C_{14}H_9O_3$ [M-H]⁻, 225.0552; found, 225.0556.
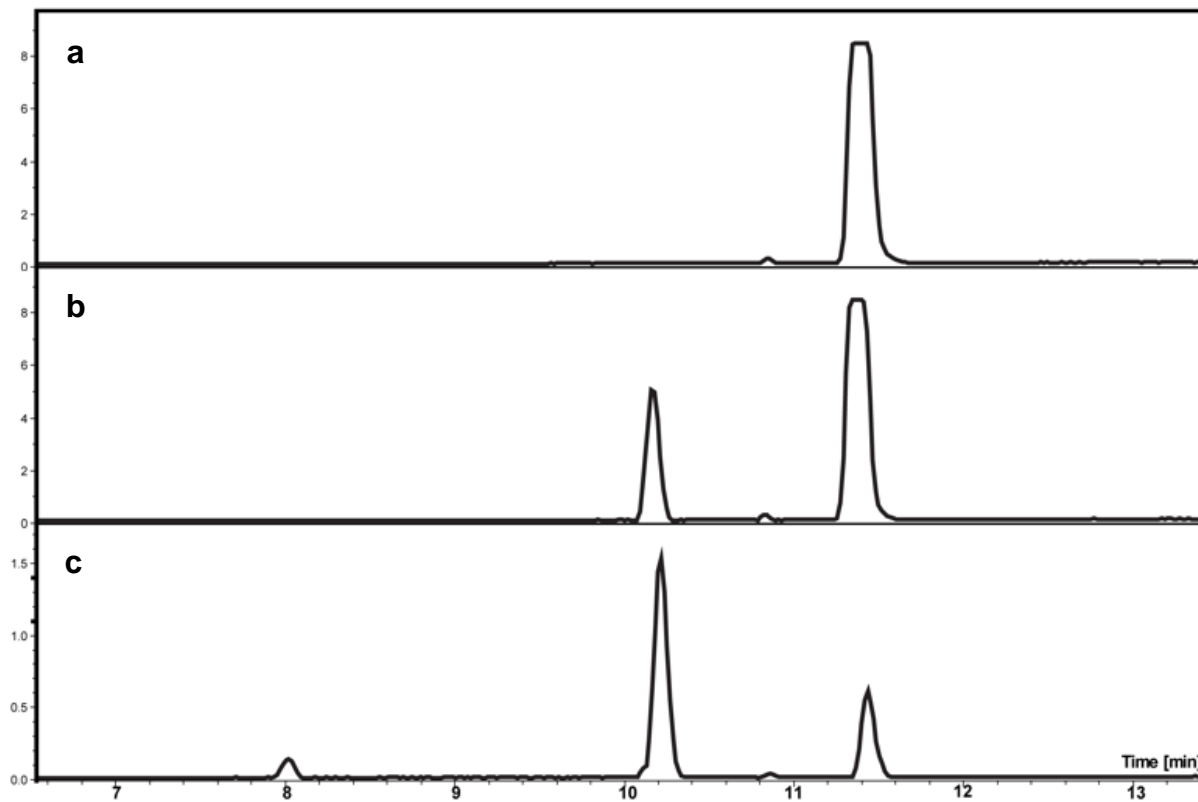
Figure S4. LC-MS traces of (a) pristine DHAQ, (b) cycled DHAQ in discharged state, and (c) synthetic DHA standard. The peak at 10.2 min was identified as DHA. The LC trace of the pure synthetic DHA standard also included a peak at 11.4 min corresponding to DHAQ due to partial oxidation during material handling in alkaline solution.
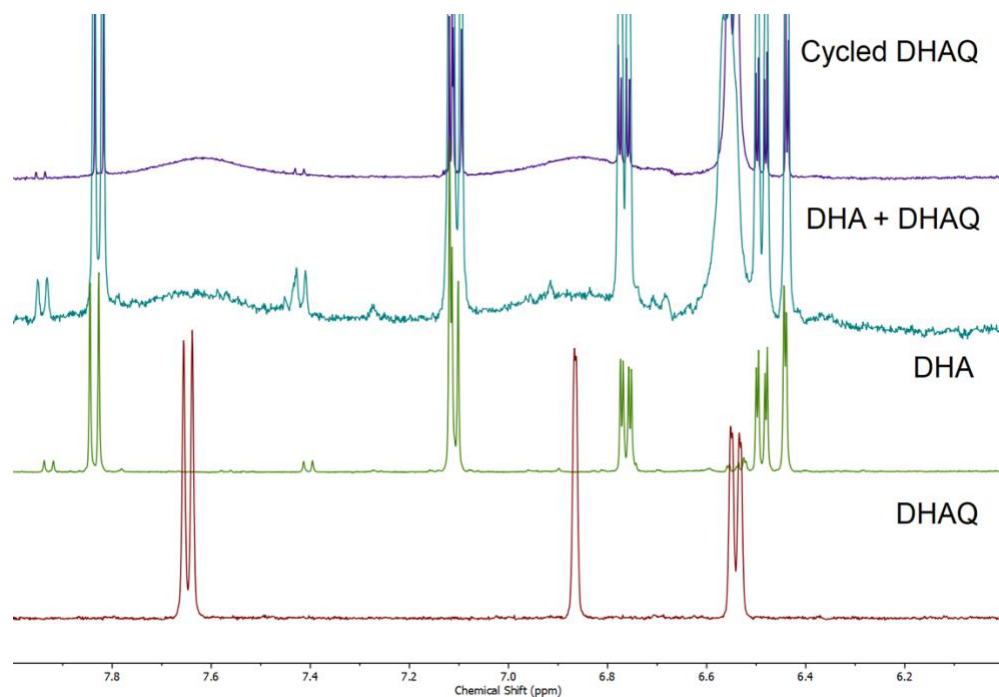
Figure S5. ^{1}H NMR spectra (500 MHz, D_2O) of DHAQ (bottom spectrum), pristine DHA (2nd spectrum from bottom), a mixture of pristine DHA and DHAQ (3rd spectrum from bottom), DHAQ cycled in a symmetric cell configuration and discharged at +200 mV oxidation potential (top spectrum). The mixed sample was prepared by diluting 40 μL of each 0.1 M electrolyte in 720 μL of D_2O, whereas all other samples were prepared as described in the Experimental Methods section.

Oxidation of DHA

A sample of cycled DHAQ electrolyte, also utilized in the experiment of which results are depicted in Fig. S2b, was discharged at +200 mV overpotential; the ^{1}H NMR spectrum revealed peaks matching those of DHA and broad peaks matching those of DHAQ (Fig. S6a, bottom spectrum). When the same electrolyte was discharged at +350 mV, the ^{1}H NMR spectrum revealed sharp (rather than broad) peaks matching those of DHAQ and peaks later confirmed to match those of (DHA)$_2$ but no peaks matching those of DHA (Fig. S6a, top spectrum). When a sample of synthetic DHA was chemically oxidized by aeration, the ^{1}H NMR spectrum indicates that most of the DHA was converted to DHAQ and a smaller amount was converted to (DHA)$_2$ (Fig. S6b).
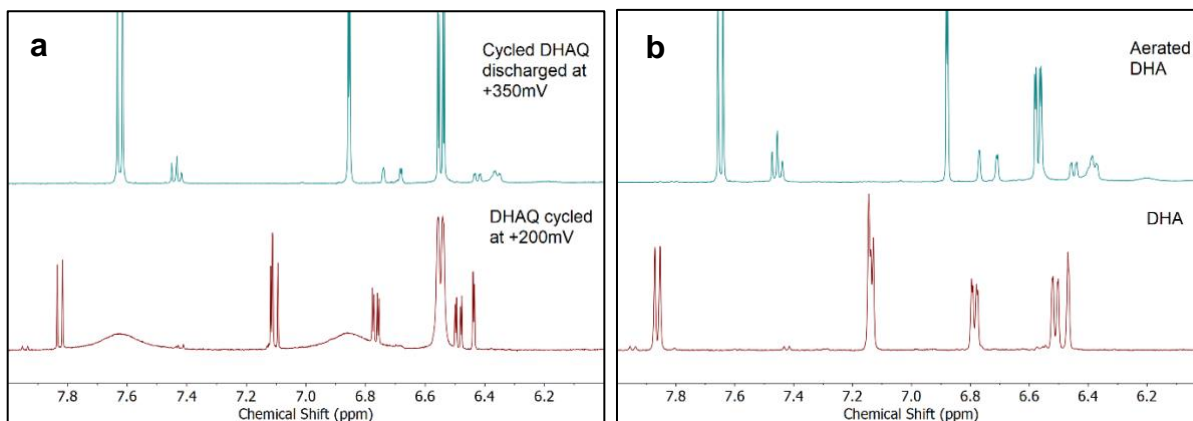
Figure S6. ^{1}H NMR spectra (500 MHz, D$_2$O) of (a) a sample of cycled DHAQ electrolyte discharged at +200 mV oxidation overpotential (bottom spectrum) and at +350 mV oxidation overpotential (top spectrum) and (b) a sample of synthetic DHA before aeration (bottom spectrum) and after aeration (top spectrum).

Formation and detection of (DHA)$_2$

HPLC-MS of a cycled DHAQ electrolyte after a strongly oxidative discharge (+350 mV) was applied, showing disappearance of DHA and the appearance of new compounds with [M-H]$^-$ = 449.1028 and [M-H]$^-$ = 223.0404.
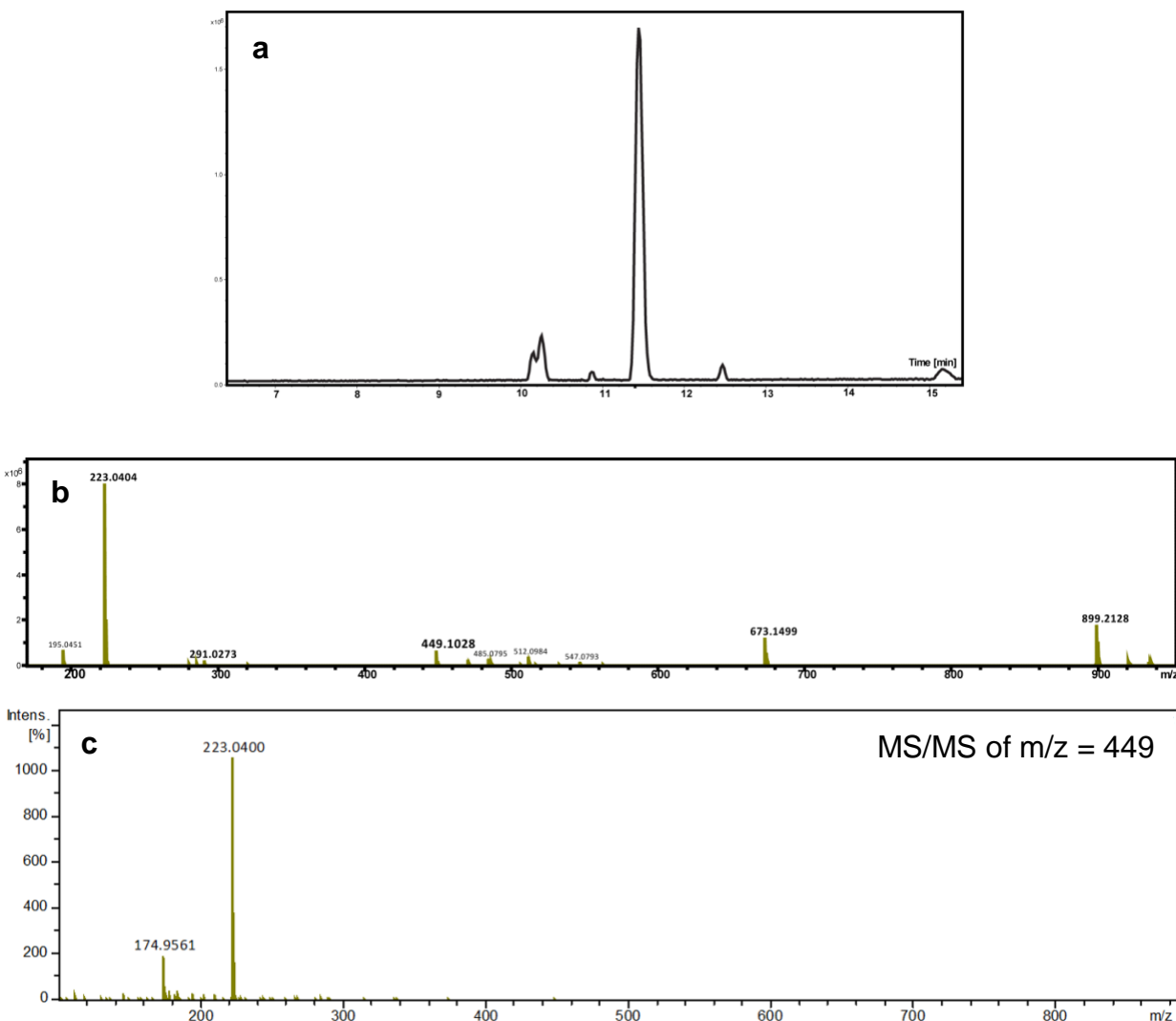
Figure S7. (a) LC-MS trace of DHAQ after prolonged cycling shows disappearance of the DHA peak and appearance of an additional peak at 10.2 min with [M-H]$^-$ of 449.1028. (b) Mass spectrum of the material eluted at 10.2 min in the LC trace. A [M-H]$^-$ of 449.1028 corresponds to a neutral molecular formula $C_{28}H_{18}O_6$. The majority of the ions existed in a fragment with [M-H]$^-$ of 223.04104. (c) The material with [M-H]$^-$ of 449.1028 was isolated and fragmented by MS/MS, indicating that the signal with [M-H]$^-$ of 223.04104 observed by LC-MS corresponds to fragments of the material with [M-H]$^-$ of 449.1028.

Identification of (DHA)$_2$

A sample with [M-H]$^-$ of 449.1028 was isolated from the DHAQ electrolyte by pHPLC (preparative HPLC), and its mass and retention time were confirmed by LC-MS. The structures were subsequently assigned as (DHA)$_2$ stereoisomers by NMR.
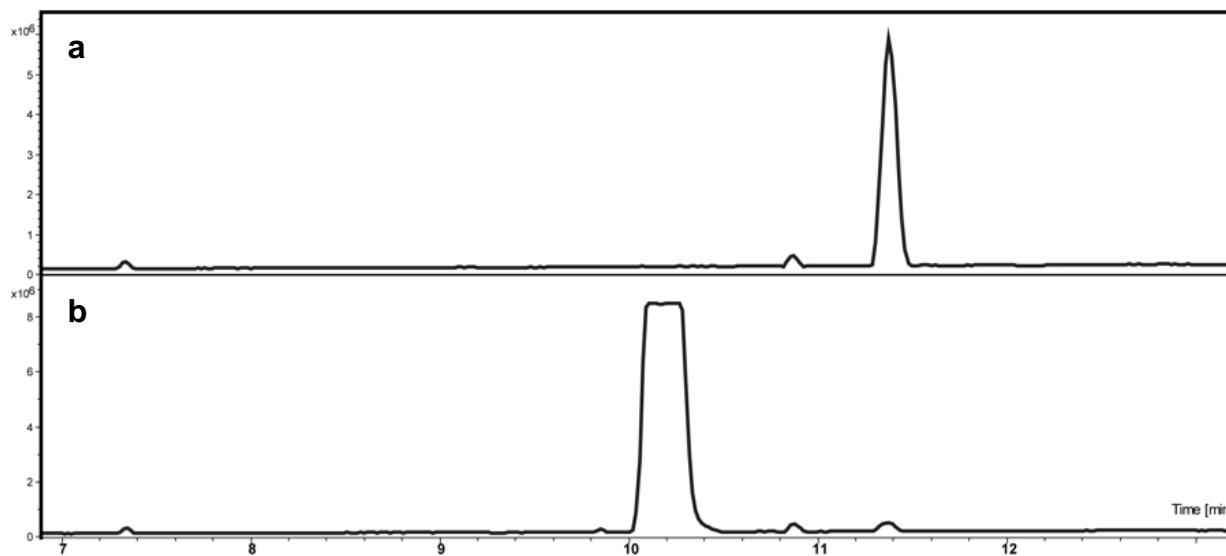
Figure S8. LC-MS traces of (a) DHAQ after pHPLC separation of cycled DHAQ electrolyte and (b) DHA dimers (DHA)$_2$ after pHPLC separation. (DHA)$_2$ is pure by LC trace: The peaks at 7.38 min and 10.83 min are due to impurities from solvents and were also present in blank samples.

Following separation from the DHAQ electrolyte by pHPLC, the sample with [M-H]$^-$ of 449.1028 was dissolved in DMSO-d_6 and analyzed by NMR to confirm the chemical structures as (DHA)$_2$ stereoisomers (Fig. S9). Full details of the NMR analysis can be found in the **Annex** at the end of the SI.

meso-di-(2,6-dihydroxy)anthrone   (*DL*)-di-(2,6-dihydroxy)anthrone
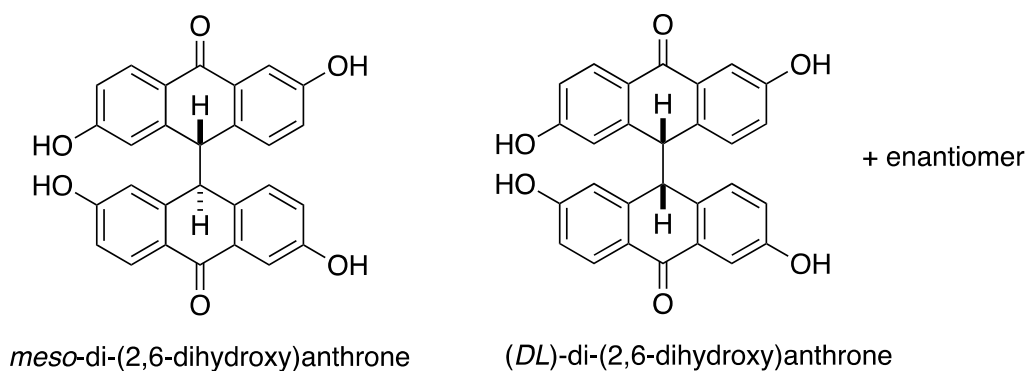
Figure S9. Chemical structures of DHAQ decomposition products, (DHA)$_2$, revealed by NMR analysis.

Time-dependence of DHA formation

Fig. S10 depicts the fraction of DHA formed from a DHAQ electrolyte in three separate experiments, identical in protocol to the one of which results are depicted in Fig. 2 and in Fig. S18-S20, but with different pause durations in each case. Taken together, these experiments suggest that the amount of DHA formed and the associated capacity loss both increase with the amount of time the DHAQ electrolyte is held in the reduced state of charge.
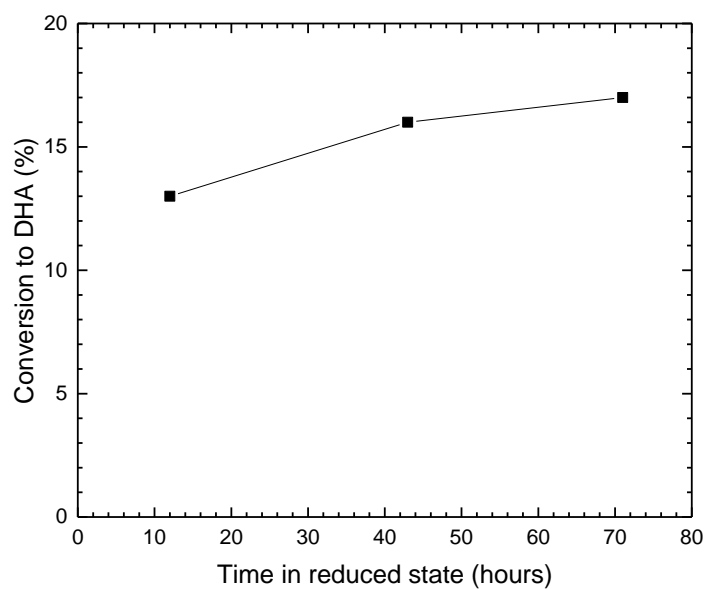
Figure S10. Amount of DHA formed during cycling pause while DHAQ electrolyte was held in reservoir in reduced state of charge.

pH dependence of DHA ^{1}H NMR spectrum

In a nitrogen-filled glovebox, an aqueous solution of 0.1 M synthetic DHA and 1.2 M KOH was prepared. An 80 µL aliquot was then dissolved in 720 µL of D_2O within a sealed 5 mm Precision Low Pressure/Vacuum Valve (LPV) NMR tube (Wilmad-LabGlass Product No. 535-LPV-7), and the ^{1}H NMR spectrum was obtained within 1 hour (top spectrum). A separate 80 µL aliquot was then dissolved in 720 µL of 1 M KOD in D_2O, and the ^{1}H NMR spectrum was obtained under identical conditions (bottom spectrum).
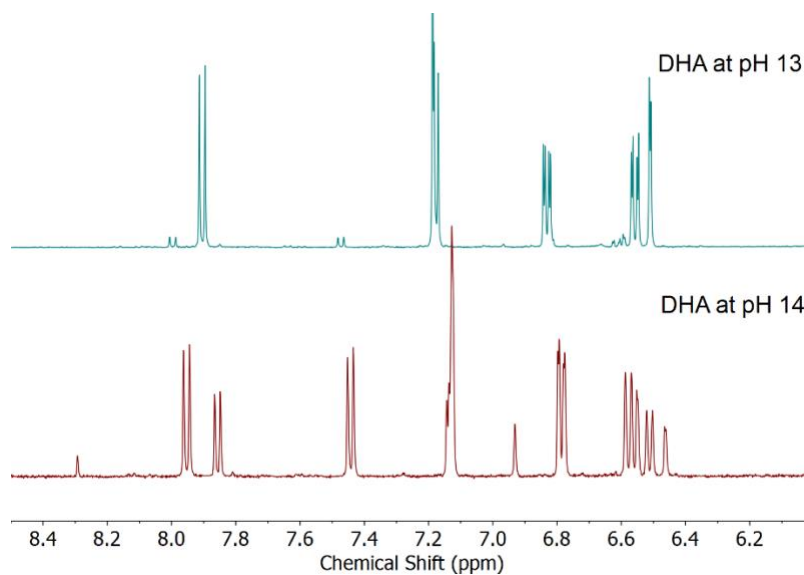
Figure S11. ^{1}H NMR spectra of DHA at pH 13 (top spectrum) and pH 14 (bottom spectrum).

Synthesis of (DHA)₂ via electrochemical oxidation of DHA

In a nitrogen-filled glovebox, an aqueous solution of 0.1 M synthetic DHA and 1.2 M KOH was prepared. An 80 µL aliquot was then dissolved in 720 µL of D_2O within a sealed LPV NMR tube, and a ^1H NMR spectrum was obtained within 1 hour (top spectrum). The DHA electrolyte was then electrochemically oxidized in a 5 cm² flow cell vs DHAQ. When the oxidation current fell below 5 mA, the cell was stopped, and another 80 µL aliquot was taken for ^1H NMR analysis.

The result below indicates that DHA was completely converted to (DHA)₂ by the electrochemical oxidation, as verified by comparison of the integrals of the ^1H NMR signals with chemical shifts of 6-8 ppm, relative to that of a sodium methanesulfonate internal standard (δ 2.6 ppm, not shown in Fig. S12).
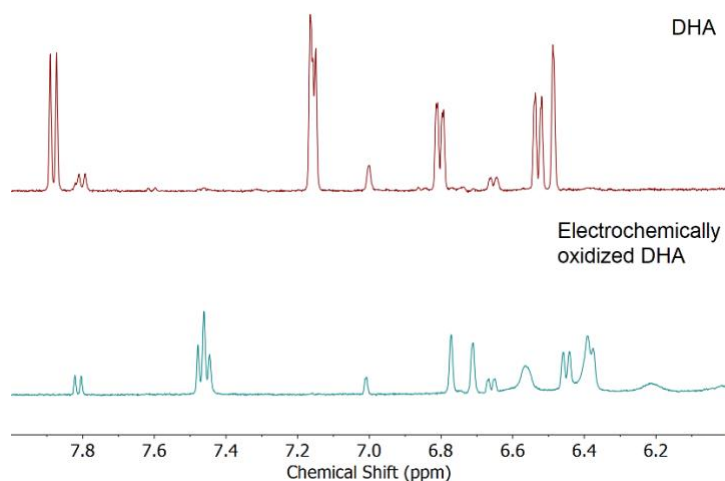
Figure S12. ^1H NMR spectra (500 MHz, D_2O) of 10 mM synthetic DHA (top spectrum) with a 5% DHAQ impurity and of the DHA electrolyte after electrochemical oxidation (bottom spectrum), demonstrating conversion of DHA to (DHA)₂. The total integral of the ^1H NMR signals with chemical shifts of 6-8 ppm, relative to that of a sodium methanesulfonate internal standard (δ 2.6 ppm, not shown), indicates complete conversion of DHA to (DHA)₂.

Recovery of DHAQ via aeration of DHA

In a nitrogen-filled glovebox, an aqueous solution of 100 mM synthetic DHA, 1 M KOH, and a 67 mM sodium methanesulfonate internal standard was prepared. Six dilutions were prepared at 10 mM DHA by diluting 10-fold in 1 M KOD in D_2O, and six dilutions were prepared at 1 mM DHA by diluting 100-fold in 1 M KOD in D_2O. Two dilutions were prepared at 10 mM DHA and pH 13 by diluting 10-fold in D_2O. The two samples at 10 mM DHA and pH 13 were prepared in sealed LPV NMR tubes, and ^1H NMR spectra were obtained. The remaining dilutions were removed from the glovebox, and samples at both DHA concentrations (10 mM and 1 mM) were oxidized by three different conditions (with two replicates performed for each condition): (1) by exposing the samples to air for several hours ("Open air"), (2) by repeatedly shaking and inverting the samples in air for less than one minute ("Air shaken"), and (3) by exposing the samples to pure oxygen from a gas tank ("O_2 bubbled"). The ^1H NMR spectra of each of these samples were subsequently obtained, and in each, the signal matching a single DHAQ proton was integrated with respect to the internal standard. For each condition, the ratio of DHAQ formed relative to initial DHA was determined by dividing this integral by twice the integral of the signal corresponding to a single proton in the ^1H NMR spectrum of unaerated DHA at pH 13 with respect to the internal standard. (The factor of two in the denominator reflects that the DHAQ proton signal corresponds to two equivalent protons, whereas the DHA proton signal corresponds to one. For each spectrum, the average integral of the two replicates was used, and the error bars in Fig. S13 correspond to the standard deviation for each condition.)
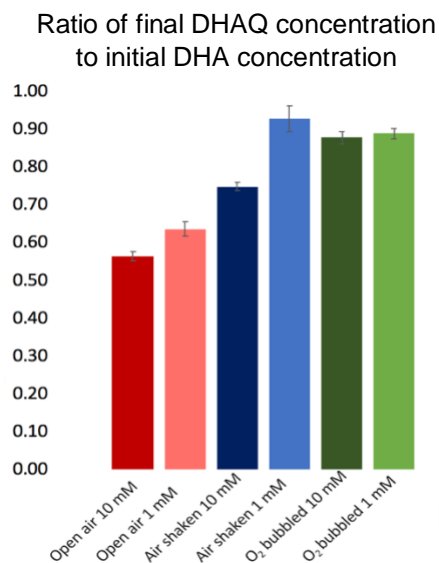
Figure S13. Dependence of fraction of DHAQ formed relative to initial DHA on initial DHA concentration and method of oxygen exposure. The data demonstrate that the fraction of DHAQ recovered varies based on the initial DHA concentration and method of oxygenation and that with sufficient oxygen exposure, greater than 90% recovery may be achieved.

Concentration dependent production of (DHA)$_2$
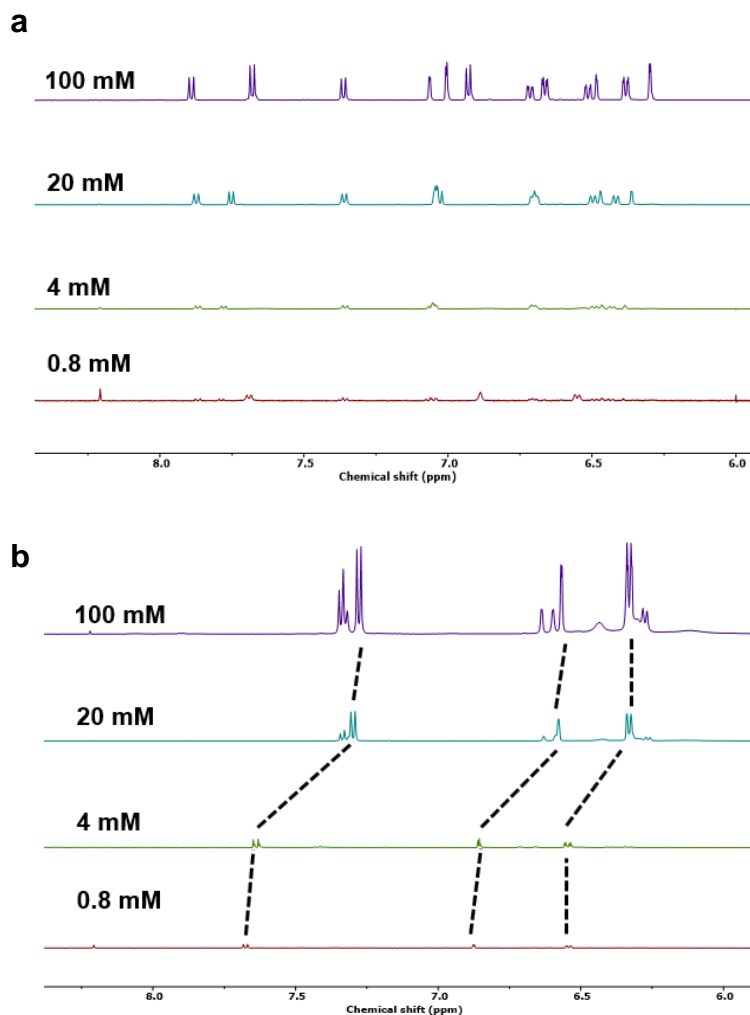
Figure S14. ^{1}H NMR spectra of (a) synthetic DHA at various concentrations dissolved in 1 M KOH solution and (b) after 1 day of exposure to air. From top to bottom: 100 mM, 20 mM, 4 mM, 0.8 mM. Dashed lines show concentration-dependent shift of DHAQ signals. The greater relative fraction of (DHA)$_2$ signals in spectra of samples formed from higher concentration DHA is consistent with a bimolecular oxidation reaction.

Concentration effects on capacity fade

Fig. S15 depicts results of an experiment in which a symmetric cell was initially cycled with 0.1 M DHAQ in a 1.2 M KOH solution, resulting in a fade rate of ~8%/day. The electrolyte was subsequently diluted 10x with 1 M KOH, some volume was removed, and cycling continued. At 0.01 M DHAQ, the cell fade was ~4.2%/day. The electrolyte was diluted 10x again with 1 M KOH, volume was again removed, and cycling continued. At 0.001 M DHAQ, the fade rate was ~1.9%/day. These differences could be due to either a decrease in the rate of disproportionation/DHA formation or due to a decrease in the dimerization rate.
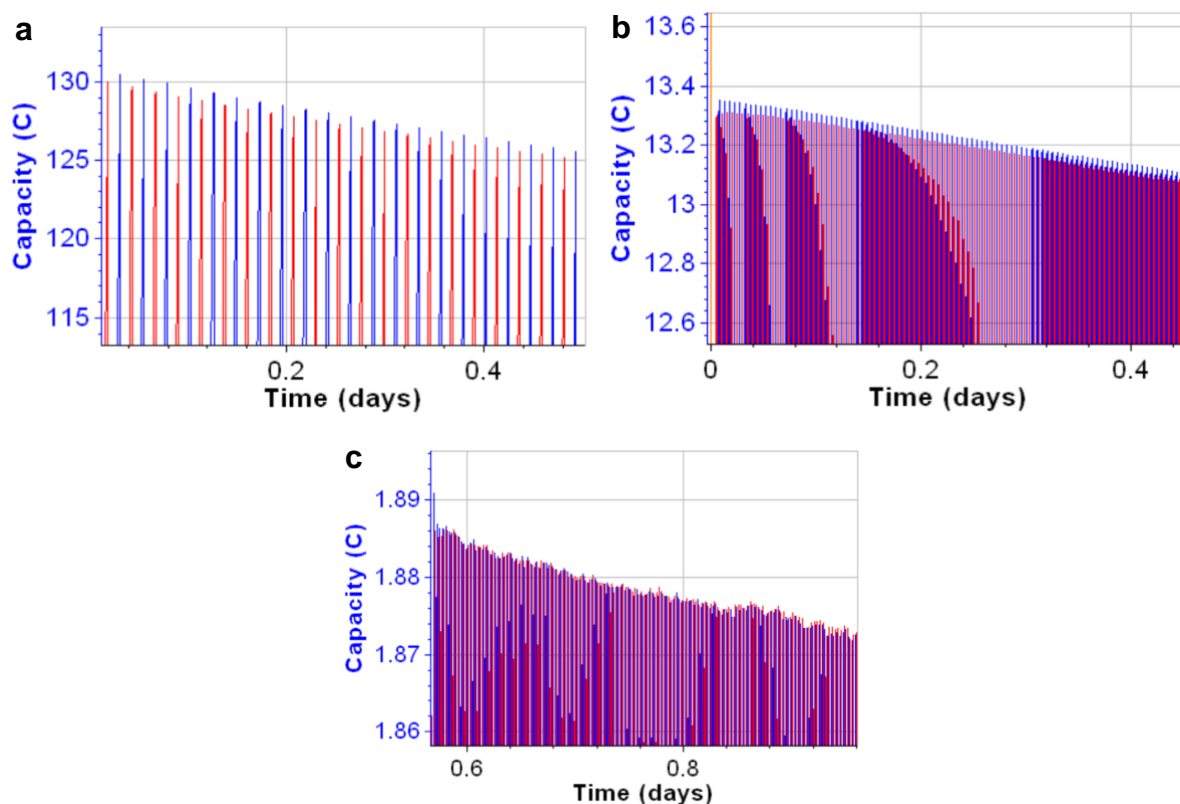
Figure S15. Symmetric cell cycling of (a) 6 mL of 0.1 M DHAQ in a 1.2 M KOH solution, showing a capacity fade rate of ~8.0%/day, (b) 6.5 mL of 0.01 M DHAQ in a 1.02 M KOH solution, showing a capacity fade rate of ~4.2%/day, and (c) 8 mL of 0.001 M DHAQ in a 1 M KOH solution, showing a capacity fade rate of ~1.9%/day.

Characteristics of (DHA)$_2$ cycling

After the 0.1 M DHA electrolyte utilized in the experiment of which results are depicted in Fig. S12 was completely converted to 0.05 M (DHA)$_2$, this electrolyte of (DHA)$_2$ was cycled galvanostatically as a posolyte against a DHAQ negolyte, with potential holds at +700 mV and -300 mV. Within these potential limits, the accessed capacity of approximately 48 C corresponds to only 2 electrons transferred per molecule of (DHA)$_2$. Although more capacity may be accessed by an even greater oxidation overpotential (according to Fig. 1B), this would result in even greater voltage efficiency loss.
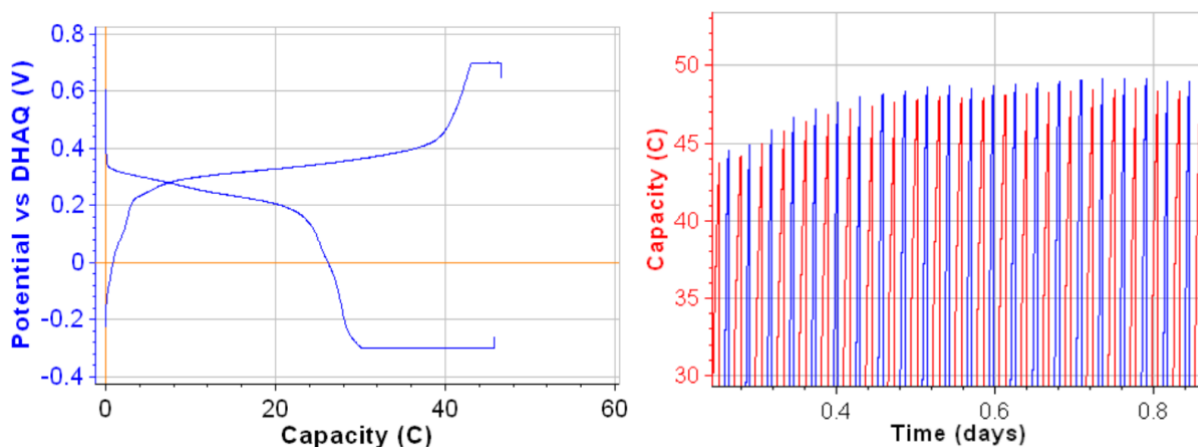
Figure S16. (a) A typical cycle from the cycling of 5 mL of 0.05 M (DHA)$_2$ in a 1.2 M KOH solution vs 0.1 M DHAQ in a 1.2 M KOH solution from -300 mV to +700 mV with 3 mA cm^{-2} current cutoff limits. (b) Change in capacity vs. time.

Stability of (DHA)$_2$

To monitor the stability of the (DHA)$_2$ dimers, an aqueous solution of 0.1 M DHA and 1.2 M KOH was prepared and aerated so that the DHA was converted to DHAQ and (DHA)$_2$. The ^{1}H NMR spectrum of an 80 μL aliquot of the solution was obtained immediately after aeration. The electrolyte was then stored for 5 days, after which an ^{1}H NMR spectrum of another aliquot was obtained, demonstrating a decrease in the integrals of the (DHA)$_2$ signals.
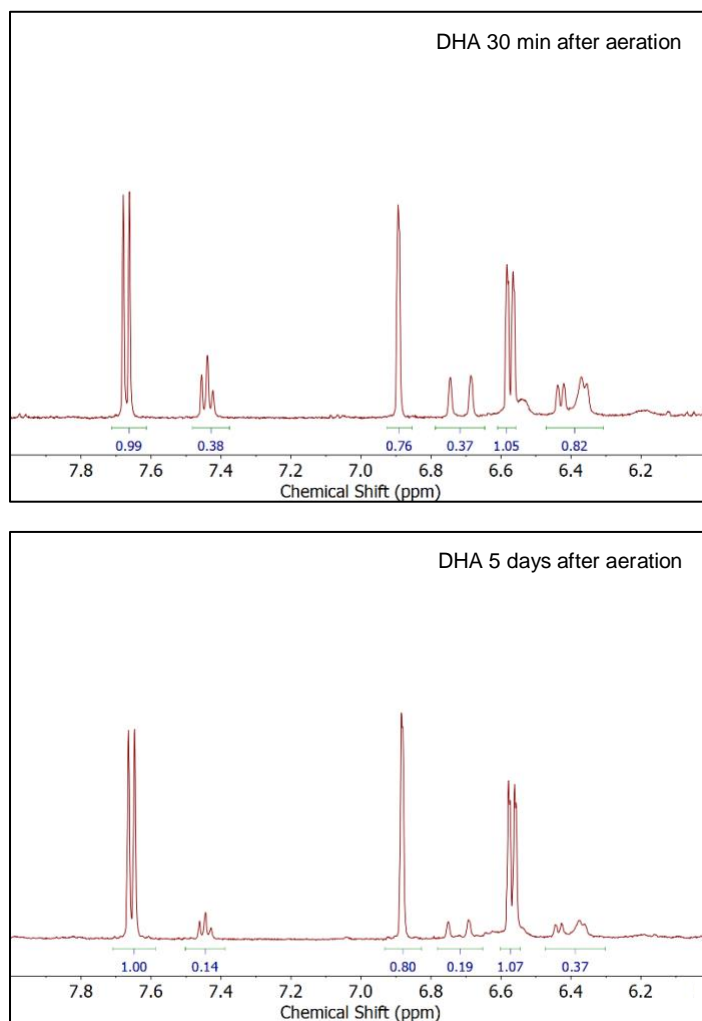
Figure S17. ^{1}H NMR spectra of DHA, 30 min (top) and 5 days (bottom) after aeration, which show a decrease in integrals of (DHA)$_2$ signals after 5 days in 1.2 M KOH solution. The integral of the signal with chemical shift of 7.45 ppm decreases from 0.38 to 0.14 vs DHAQ, reflecting a loss of over 50%.

Quantitative analysis of DHA and (DHA)$_2$ formation and correlation with capacity loss

Fig. 2 and Fig. S18 depict results of an experiment to quantitatively correlate the formation of DHA and subsequent dimerization with capacity loss, which demonstrates the formation of DHA when a DHAQ electrolyte was held in the reduced state of charge. An aliquot of electrolyte (Aliquot #1) was removed at the beginning of a pause in cycling. Though not shown due to scale, the first step after the pause is another reduction step involving 18 C (or 16% of the total capacity before the pause), consistent with the disproportionation reaction involving the oxidation of DHAHQ. In this case, the 43 hour pause in the reduced state of charge converted 16% of the DHAHQ into DHA before cycling was resumed. DHA was not oxidized by the first discharge cycle after the pause when +200 mV was applied (Aliquot #2) but was completely converted to (DHA)$_2$ when +350 mV was applied (Aliquot #3). Overall, the cycling capacity decreased by 27 C during the pause, a loss of 23%, corresponding to approximately 15% after correcting for the aliquots removed for ^{1}H NMR analysis. This capacity loss correlates well with the 16% loss of DHAQ concentration and transient formation of DHA during the pause and with the conversion of DHA to (DHA)$_2$ thereafter (see Fig. S19). This experiment was repeated twice with different electrolyte samples utilizing 12 hour and 71 hour pauses. The DHAQ concentration loss measured by ^{1}H NMR was 13% during the 12 hour pause and 17% during the 71 hour pause (see Fig. S10).
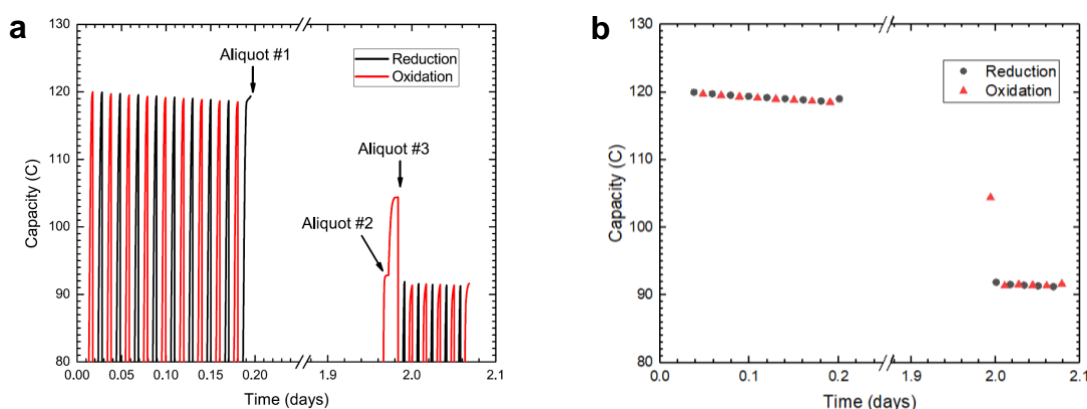
**Figure S18.** Capacity fade observed when redox cycling was paused in the reduced state of charge. Both figures depict the same data as depicted in Fig. 2 but plotted as (a) complete charge and discharge curves and (b) absolute capacity. After 8 cycles, cycling was stopped once the reduction current reached its limit, pumping was stopped with the electrolyte stored in its reservoir, and Aliquot #1 was removed (and immediately aerated). Cycling was resumed after 43 hours, and the first oxidative discharge after the pause was performed in two steps. First, the sample was discharged at +200 mV overpotential, at which point Aliquot #2 was removed, and then the discharge was continued at +350 mV until the current limit was reached, at which point Aliquot #3 was removed. The capacity accessed after this discharge was proportional to the remaining concentration of DHAQ (when adjusted for removal of the aliquots).
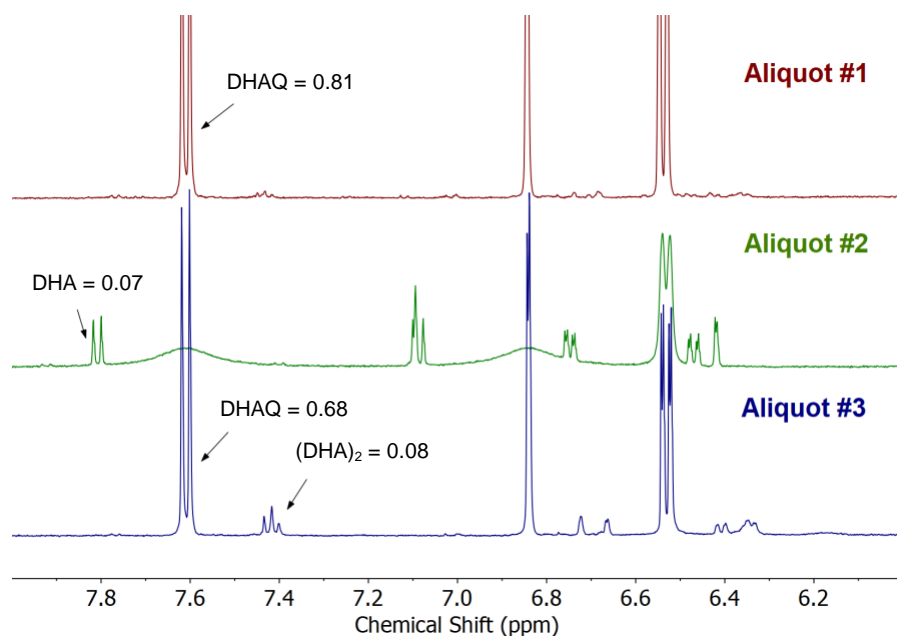
Figure S19. Quantitative electrolyte species tracking by ^{1}H NMR (aliquots defined in caption of Fig. S18), where numbers in black correspond to signal integrations relative to that of an internal standard of sodium methanesulfonate (δ 2.6 ppm, not shown). The integral of the DHA signal (one proton) with a chemical shift of 7.82 ppm is 0.07, whereas that of the DHAQ signal with a chemical shift of 7.62 ppm (two protons) has decreased by 0.13 after the DHA has been fully converted to (DHA)$_2$. Hence, the loss of DHAQ concentration is due to DHA formation. The (DHA)$_2$ signals with chemical shift near 7.42 ppm (two protons total for each dimer) have an integral of approximately 0.08 as well. Hence, all DHA appears to be electrochemically oxidized to (DHA)$_2$ (as demonstrated in Fig. S12). From the initial spectrum to the final (DHA)$_2$ spectrum, nearly all protons in the region shown are conserved, demonstrating that the loss of DHAQ has been mass-balanced by conversion to DHA and subsequent conversion to (DHA)$_2$.
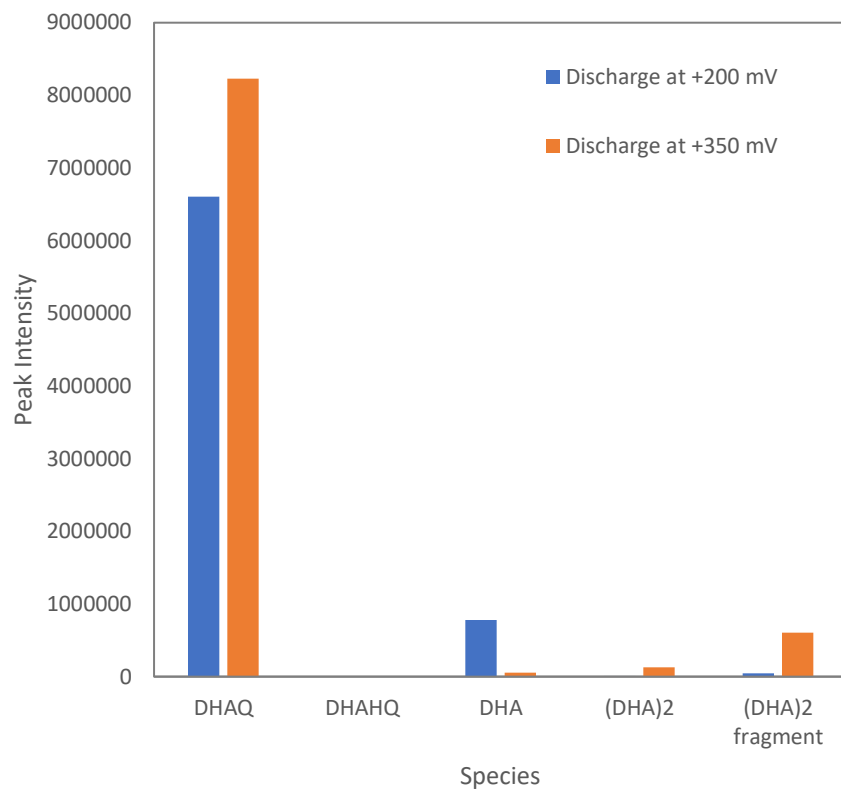
Figure S20. Corroboration by HPLC-MS of quantitative ^{1}H NMR analysis of electrolyte species depicted in Fig. S19. After discharging at +200 mV (blue), substantial amounts of DHA remain, whereas the DHAHQ has been fully converted to DHAQ. After discharging at +350 mV (orange), both (DHA)$_2$ and the fragment with [M-H]$^-$ of 223.04104 described in Fig. S7 appear in substantial quantities.

DHA formation vs state of charge of DHAQ

The state of charge (SOC) limit of the DHAQ electrolyte was demonstrated to strongly influence the cycling capacity fade rate. To directly quantify the relationship between capacity fade rate and SOC limit, an aqueous electrolyte comprising 0.1 M DHAQ and 1.2 M KOH was charged in an oxygen-free glovebox to approximately 90, 80, 70, and 60% SOC (DHAHQ relative to total DHAQ + DHAHQ). Slow charging was performed potentiostatically at a minimal value of 1.25 V in order to avoid overcharging the electrolyte in proximity to the electrodes. In order to reach 90% SOC, the potential was increased to 1.3 V near the end of charge to reach the desired SOC. Within 1 hour of charging, aliquots were diluted with D_2O in sealed LPV NMR tubes, and the ^1H NMR spectra were obtained without exposure to oxygen. The resulting spectra (Fig. S21) depict broadening of the peaks corresponding to DHAQ, whereas those corresponding to DHA are sharp and diminishing in area as the SOC is decreased (spectrum at 60% SOC not shown due to lack of quantifiable peaks). When quantified relative to a sodium methanesulfonate internal standard (δ 2.6 ppm, not shown), the amount of DHA observed at 70% SOC is approximately 33% and 16% of the amount observed at 80% and 90% SOC, respectively. Although an exact correspondence with a cycling fade rate cannot be established due to variable charging conditions and the time dependence of DHA formation, this result demonstrates the sensitivity of DHA formation to SOC and is consistent with the proposed disproportionation reaction described in the main text.
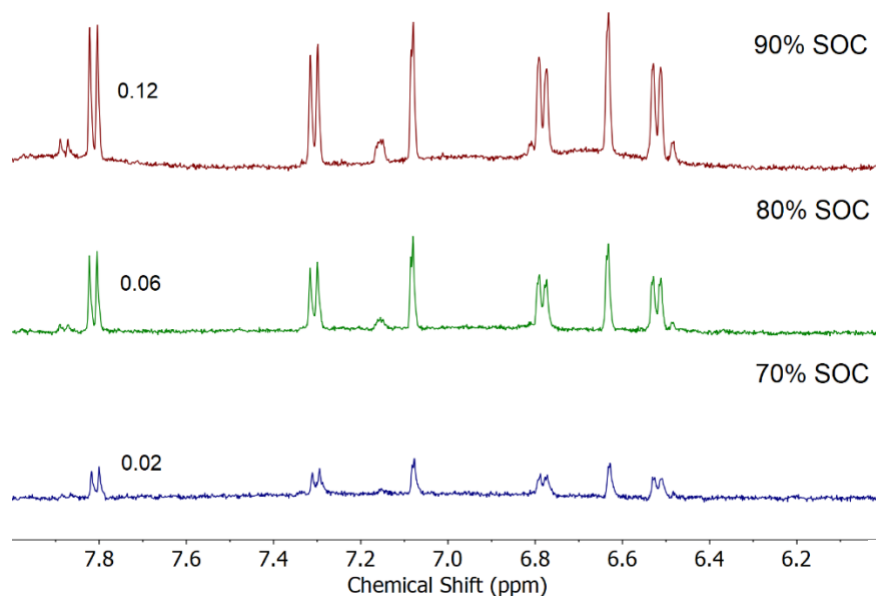
Figure S21. Relative concentration of DHA at different SOC of DHAQ. Integration of signals with chemical shift of 7.8 ppm reflect the relative quantities of DHA vs a sodium methanesulfonate internal standard (δ 2.6 ppm, not shown).

Capacity fade mitigation strategies

Fig. S22 below contains the same data as depicted in Fig. 4 in the main text but plotted as absolute capacity rather than relative capacity.
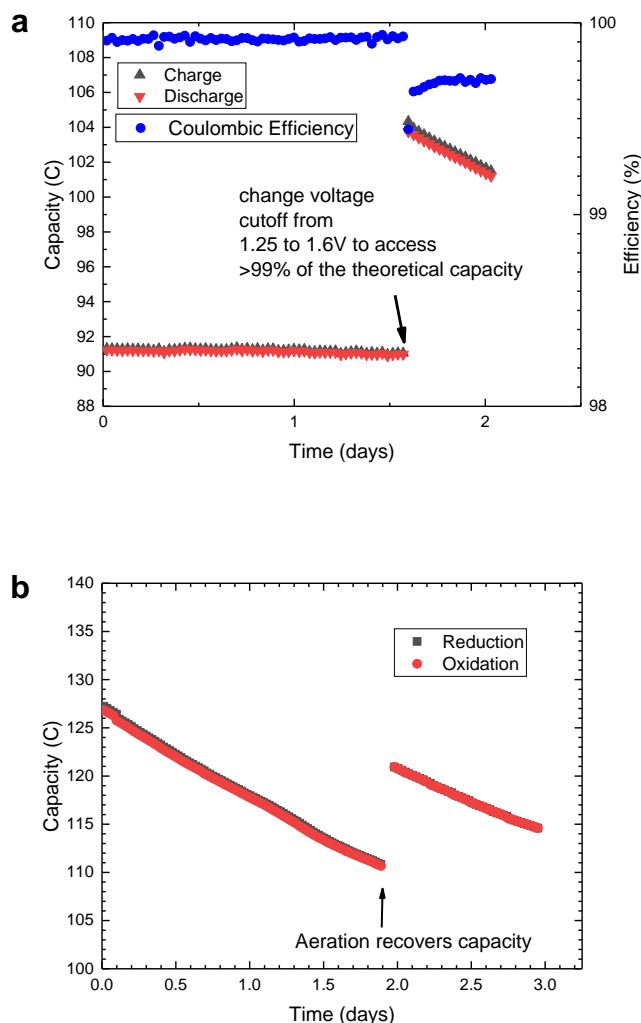
Figure S22. (a) Limiting the state of charge reduces the rate of capacity loss in a negolyte-limited DHAQ-Fe(CN)$_6$ full cell. Over the first 1.6 days, the operating state of charge was limited to 88% of the theoretical capacity (i.e., 88% DHAHQ and 12% DHAQ), and the capacity faded at only 0.14%/day. The right-hand segment reflects typical operating conditions (cycling to 99.9% of theoretical capacity), and the capacity faded at 5.6%/day. (b) Symmetric cell cycling in which the capacity-limiting side (5 mL of 0.1 M DHAQ in a 1.2 M KOH solution) demonstrates recovery of 70% of lost capacity after aeration of discharged electrolyte.

Potentiostatic cycling with Coulombic SOC cutoff

Fig. S23 depicts results of an experiment in which 1.6 V potentiostatic cycling was initially performed until the current was < 2 mA/cm^2, corresponding to the first segment of the graph. The cell lost 10 C in 2 days of full cycling, corresponding to approximately 4.8% loss per day. Then, in the second segment of the graph, the same voltage (1.6 V) was applied for charging with a Coulomb cutoff set at 95 C (88% SOC based on the 107.8 C capacity from the end of the first segment). The cell was fully discharged every cycle at 0.6 V until the current was < 2mA/cm^2. The cell lost 2 C over 2 days. This number is calculated by the capacity at the end of the first segment minus the capacity at the beginning of third segment. Using 107.8 C as the initial value, this represents approximately 0.8%/day, much less than 4.8% loss per day, which demonstrates the effect of SOC control. Although the SOC range is similar to that shown in Fig. 4A of the main text, the fade rate is higher in this case. We hypothesize that the fast charging rate due to the 1.6 V potentiostatic condition creates a local SOC gradient near the electrodes and in the tubing, which exceeds the target SOC and therefore accelerates the decomposition.
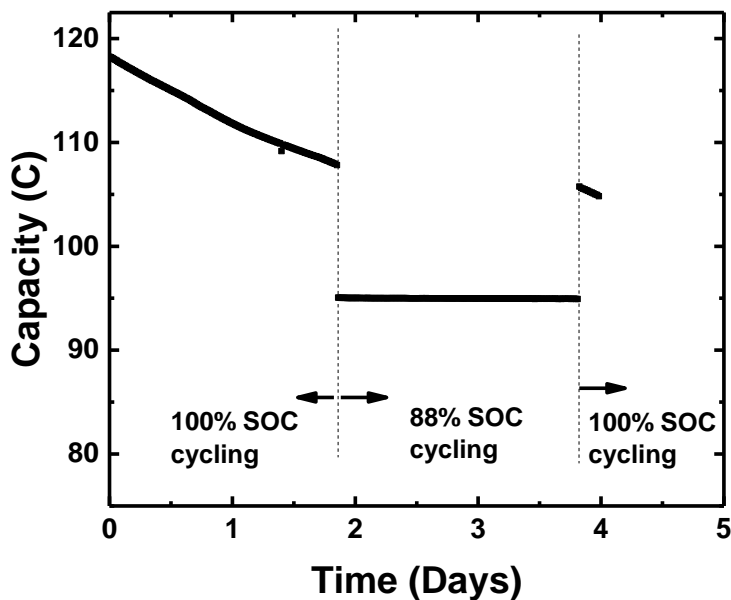
Figure S23. Potentiostatic full cell cycling of 0.1 M DHAQ in a 1.2 M KOH solution vs 0.05 M K$_4$[Fe(CN)$_6$] in a nitrogen atmosphere.

Cycling of DHAQ under aerobic conditions

As described in the main text, DHAQ capacity recovery can be achieved by aeration of the electrolyte. Alternatively, this strategy could be achieved by operation of the flow battery in an open-air environment, which also achieves a lower capacity fade rate and is demonstrated in Fig. S24. In this case, the 'protective' effect of oxygen may be due to the aeration of DHA and recovery of DHAQ, as previously demonstrated, but may also be due to the oxidation of DHAHQ, which would decrease the accessed SOC and, correspondingly, the driving force for DHA formation. In either case, this method comes at a performance cost because it engenders a loss of current efficiency due to the continuous oxidation of the negolyte. For this reason, the method of aeration after discharge demonstrated in Fig. 4 is preferable and could be achieved most effectively in an industrial application by adding an oxygen treatment step after each discharge of the electrolyte.
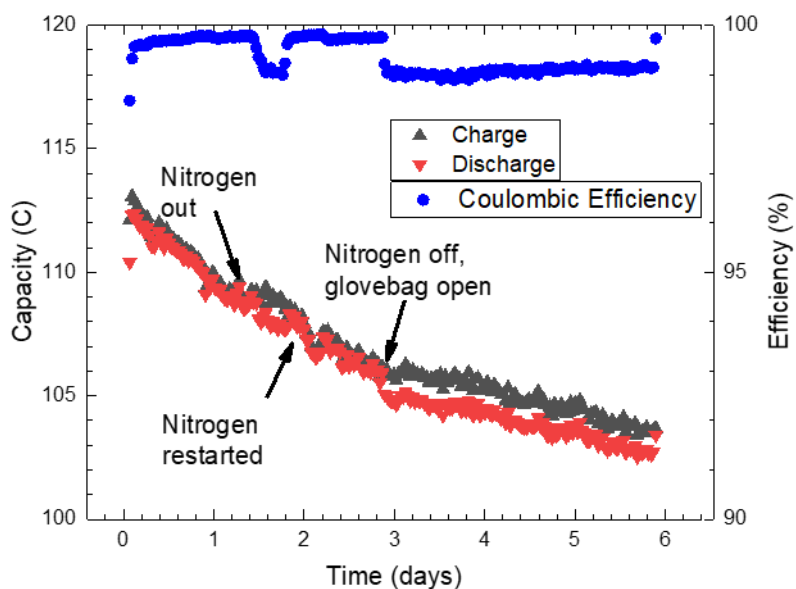
Figure S24. Potentiostatic full cell cycling of 0.1 M DHAQ in a 1.2 M KOH solution vs 0.05 M K$_4$[Fe(CN)$_6$] in a nitrogen atmosphere (fade rate = 2.8%/day) for 1 day, followed by an intermittent nitrogen atmosphere for 2 days due to dewar replacement, and then an ambient air environment (fade rate = 0.75%/day) for the final 3 days.

Theoretical investigation of anthrone formation susceptibility

The values plotted in Fig. 3 in the main text were generated as follows. For a set of para-quinone molecules taken from Ref. 41 (of the main text), all possible anthrone forms were generated. For each molecule, up to 20 conformers were generated using the RDKit;[3] these were optimized at the PM7 COSMO level of theory.[4] We then calculated the energy difference of the lowest energy anthrone form and the hydroquinone form and report this energy relative to that of DHAHQ $\rightarrow$ DHA. The raw data for these calculations is provided on figshare with the following DOI: 10.6084/m9.figshare.7455338. An excel spreadsheet listing the molecules along with their calculated properties is attached and a zipped version of the conformer and PM7 COSMO calculations is provided.

In previous works,[5] we have compared the accuracy of different quantum chemical methods (upon calibration) in predicting the thermodynamic quantities of reactions associated with redox-active organic molecules, in particular quinones. Previously, we found that both DFT (B3LYP/6-311+G(d,p) with PCM calculated at the B3LYP/6-31+G(d) optimized geometry) and PM7 COSMO give comparable results for predicting the two-proton two-electron reduction potential of quinones (mean absolute deviations of 0.04 V and 0.07 V, for B3LYP/6-311+G(d,p) with PCM and PM7 COSMO, respectively). In addition, we found for a set of ketone-gem diol equilibrium constants, the mean absolute deviations in the calculated base-10 logarithm of this equilibrium constant was 0.99 for B3LYP/6-311+G(d,p) with PCM and 1.23 for PM7 COSMO. This corresponds to an error in the reaction energy of about 6.7 kJ mol^{-1} for PM7 COSMO. Given the scale of the quantities being examined in this study, PM7 COSMO strikes the best balance between speed and accuracy.

Annex (Details of NMR spectroscopic analysis)

Characterization of DHA
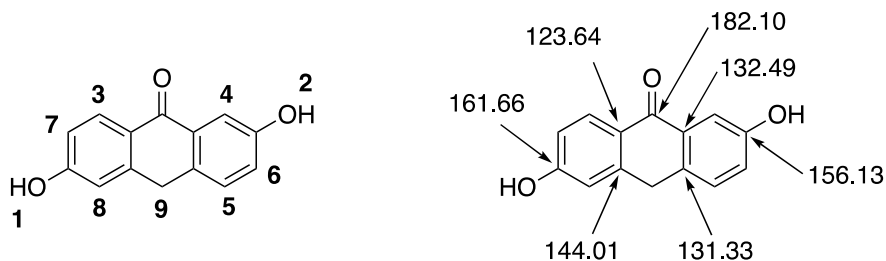
#	^{1}H (ppm)	^{13}C (ppm)	Type	Hs
1	10.40	--	br s	1
2	9.67	--	br s	1
3	8.02	129.33	d	1
4	7.51	111.27	m	1
5	7.35	129.99	d	1
6	7.06	120.95	d	1
7	6.88	115.39	m	1
8	6.86	113.91	m	1
9	4.21	31.04	s	2
500 MHz, DMSO-d_6, 25 °C Quaternary Carbons: 182.10, 161.66, 156.13, 144.01, 132.49, 131.33, 123.64 ppm				

Assignments were made by COSY, HSQC, and HMBC experiments. (Note: on a timescale of hours in DMSO, this compound tautomerizes to its phenolic form.)

Characterization of (DHA)$_2$

Dimerization of the DHA monomer with no absolute or relative stereocontrol would result in the following mixture:

meso-di-(2,6-dihydroxy)anthrone

(DL)-di-(2,6-dihydroxy)anthrone
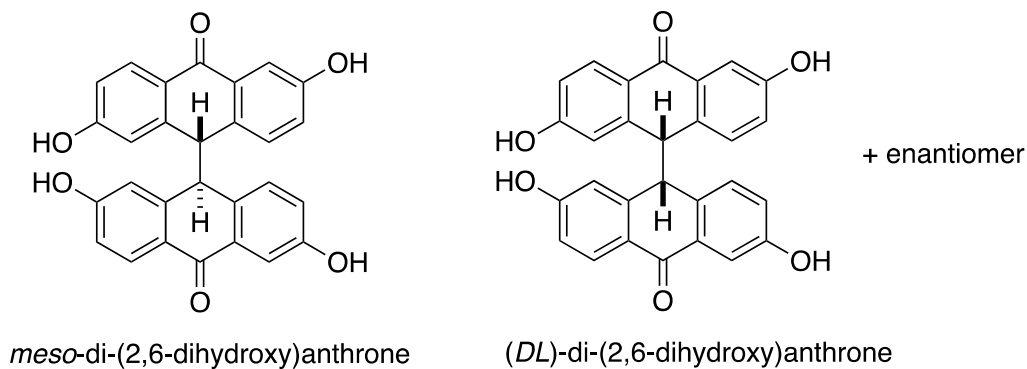
+ enantiomer

In the *meso* compound, there are two homotopic protons/carbons per site. For the pair of enantiomers, each such pair is formally diastereotopic:

(DL)-gauche⁻ (+0.5 kcal/mol)

(DL)-gauche⁺ (+0.6 kcal/mol)

diastereotopic

meso-gauche⁻ (+0.7 kcal/mol)

meso-gauche⁺ (+0.0 kcal/mol)

homotopic
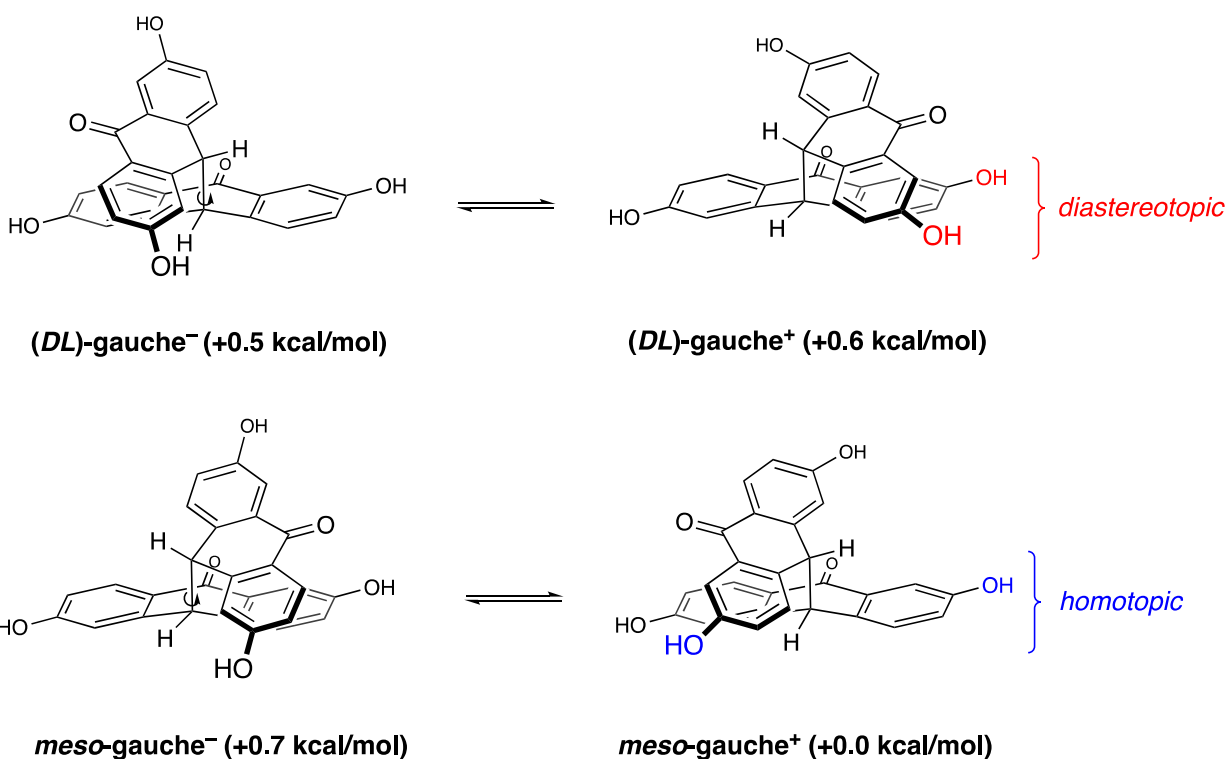
DFT calculations predict that each stereoisomer exists as a mixture of rotamers about the inter-ring bond (electronic energies, B3LYP-D3(BJ)/cc-pVTZ/PCM(DMSO) // B3LYP/6-31G*/PCM(DMSO)). In the *meso* form, rotation is a chemical exchange process between isochronous sites. In the *DL* form, to a very good approximation (see predictions below), rotation converts the diastereotopic partners into one another.
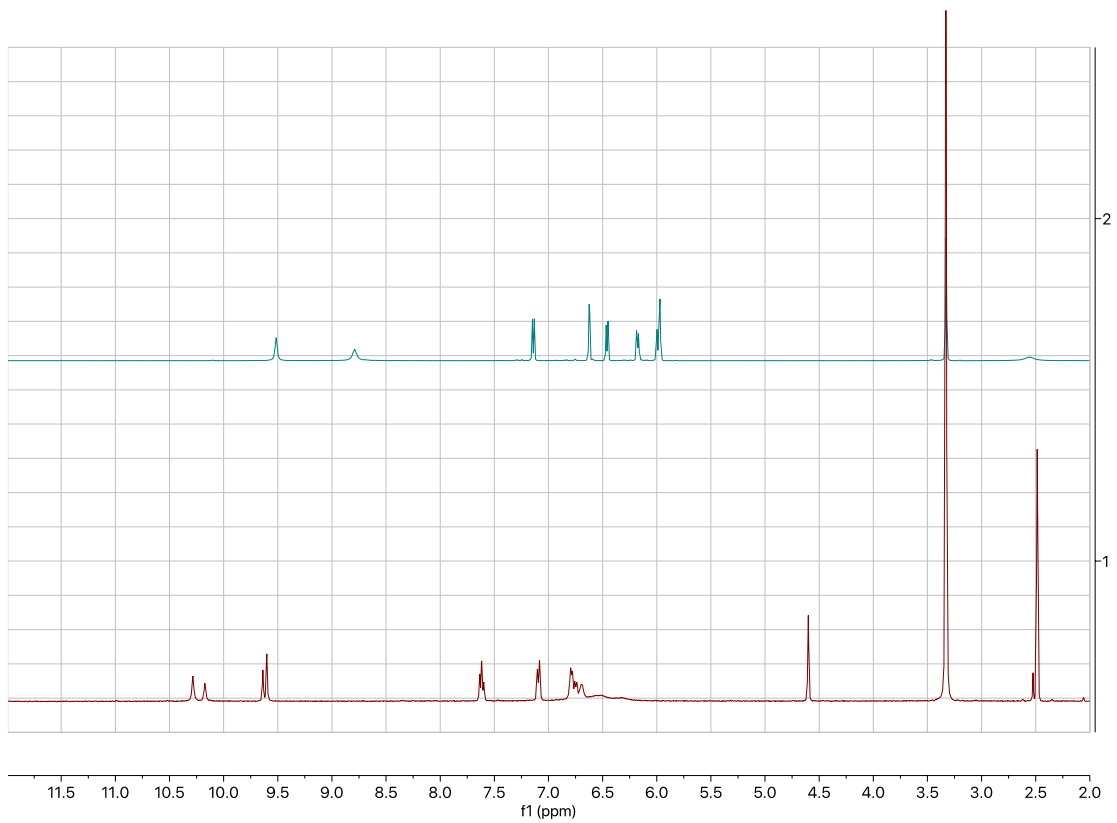
Figure S25. ^{1}H NMR spectra at 25 °C, showing that each peak is doubled (top, monomer; bottom, dimer).
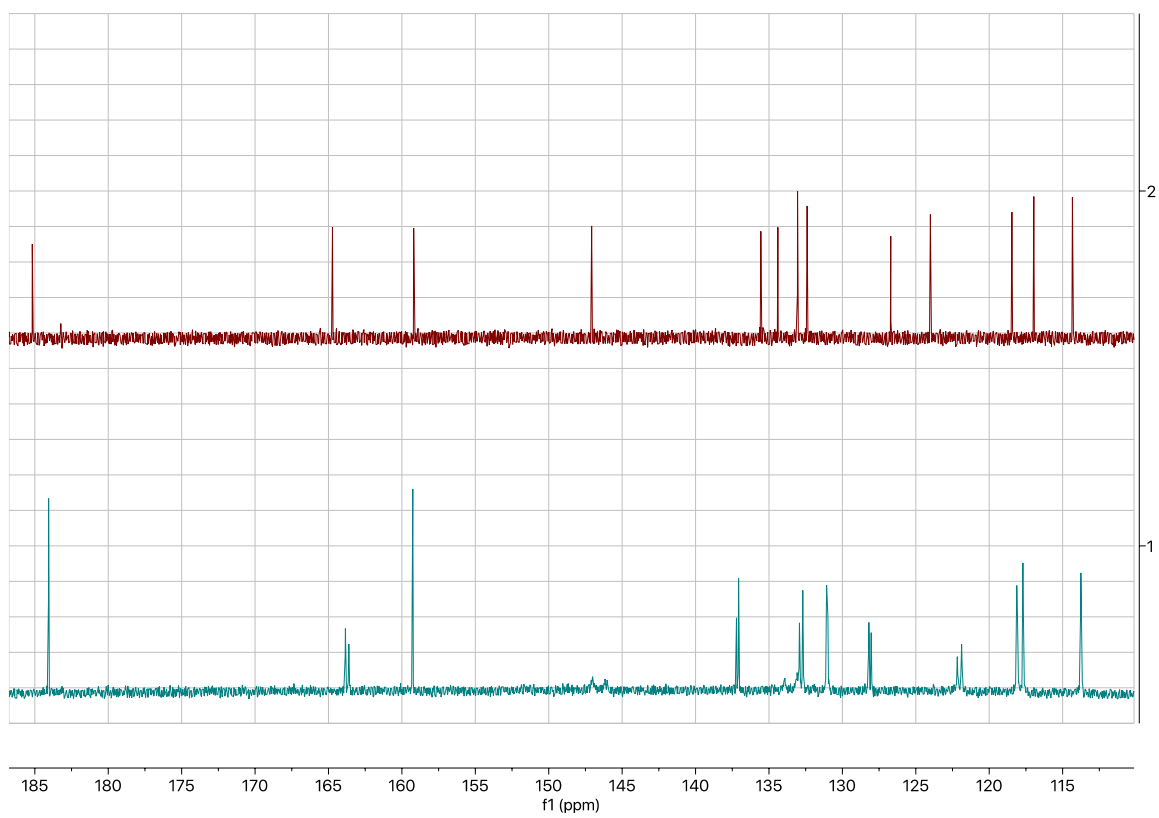
Figure S26. ^{13}C NMR spectra at 25 °C, also showing that each peak is doubled (top, monomer; bottom, dimer).
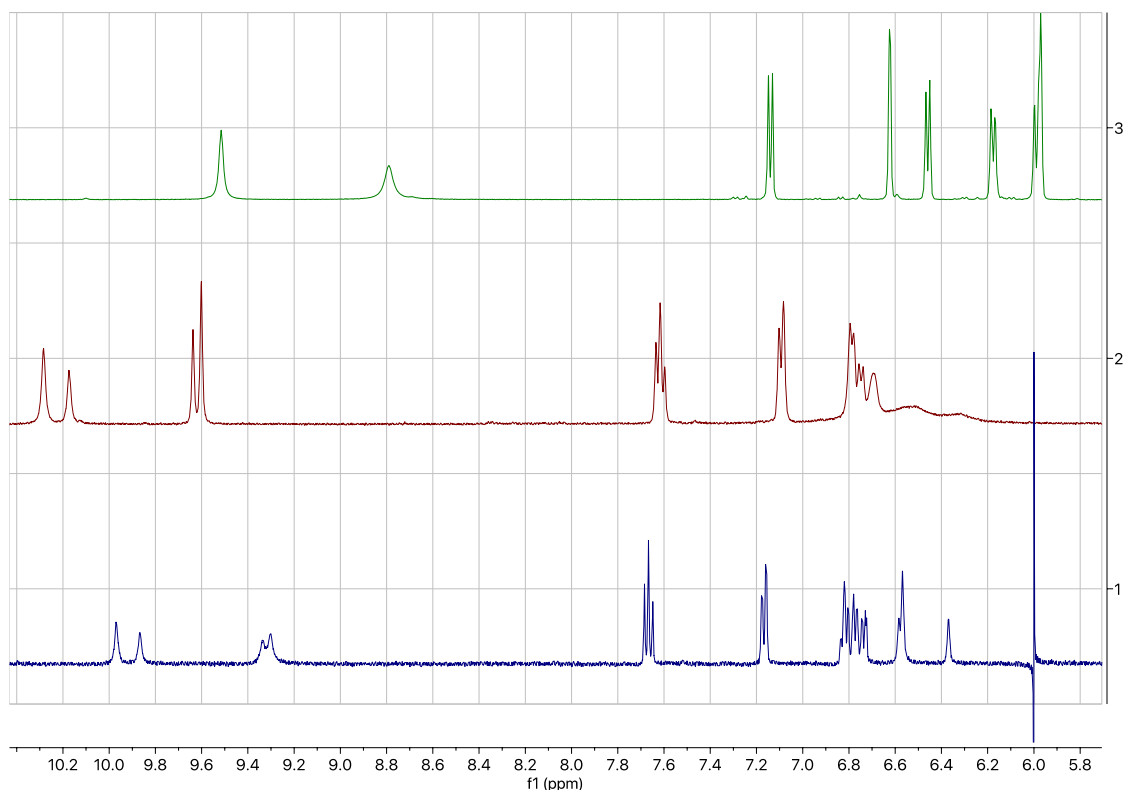
Figure S27. ^{1}H NMR spectra of (DHA)$_2$, showing further evidence of chemical exchange (top, monomer at 25 °C; middle, dimer at 25 °C; bottom, dimer at 85 °C).

Comment about rotational barrier:

Consistent with these spectra, DFT calculations also indicate that rotation has a much larger effect on chemical shift than stereoisomerism does (i.e., *meso* vs *DL*). First, the GIAO method was used to obtain isotropic shifts for DHA at PBE0-D3(BJ)/cc-pVTZ/PCM(DMSO) using B3LYP-D3(BJ)/6-31G*/PCM(DMSO) geometries. These isotropic shifts were then linearly scaled to experimental shifts:

Proton shifts					
NMR numbering	Expt (ppm)	Isotropic (ppm)	g16 numbering	Scaled (ppm)	Squared error
3	8.02	22.6447	16	8.18	2.60E-02
4	7.51	23.2813	19	7.61	9.97E-03
5	7.35	23.6088	11	7.32	1.16E-03
6	7.06	24.0612	18	6.91	2.26E-02
7	6.88	24.1366	17	6.84	1.43E-03

8	6.86	24.2871	15	6.71	2.34E-02
9	4.21	26.9419	26,27	4.32	1.30E-02
			slope	-0.8976352819	
			intercept	28.50798478	
			RMSE	0.118	

Carbon shifts	Expt	Isotropic	g16	Scaled	Squared
NMR numbering	(ppm)	(ppm)	numbering	(ppm)	error
	161.66	19.9624	1	161.4874943	2.98E-02
	113.91	70.5064	2	112.4147251	2.24E+00
	144.01	35.939	3	145.9759399	3.86E+00
	123.64	59.2896	4	123.3050274	1.12E-01
	129.33	51.2334	5	131.1267281	3.23E+00
	115.39	69.3048	6	113.581349	3.27E+00
	182.1	-0.8124	7	181.6575831	1.96E-01
	132.49	50.3083	8	132.0249004	2.16E-01
	131.33	49.2537	9	133.0488032	2.95E+00
	129.99	51.9599	10	130.421375	1.86E-01
	120.95	63.4898	12	119.2270864	2.97E+00
	156.13	25.7197	13	155.8977774	5.39E-02
	111.27	71.7596	14	111.1980031	5.18E-03
	31.04	153.4626	25	31.87320755	6.94E-01
			slope	-0.9708920795	
			intercept	180.8688304	
			RMSE	1.195717902	

These scaling factors were then used to predict the shifts for both rotamers of the *DL-* and *meso-*forms. Canonical atom numbering was used:
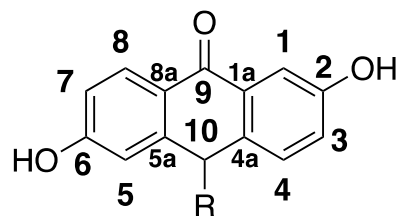
canonical numbering

| atom number | predicted shifts (ppm) meso | | DL | | | | (unsigned) average gauche - vs + difference | | averages | | gauche - vs + | meso vs DL |
| | | | gauche minus | | gauche plus | | | | | | | |
	gauche minus	gauche plus	ring 1	ring 2	ring 1	ring 2	meso	DL	meso	DL	difference	difference
1	6.994	7.414	7.297	6.997	6.998	7.295	0.420	0.299	7.204	7.147	0.359	0.057
3	6.256	7.079	7.044	6.258	6.262	7.044	0.823	0.784	6.667	6.652	0.804	0.015
4	5.672	7.718	7.704	5.541	5.545	7.705	2.046	2.161	6.695	6.624	2.103	0.071
5	7.240	4.713	4.858	7.266	7.257	5.089	2.527	2.288	5.977	6.118	2.408	0.141
7	6.755	6.569	6.599	6.787	6.771	6.466	0.186	0.247	6.662	6.656	0.216	0.006
8	7.741	7.557	7.551	7.852	7.846	7.520	0.184	0.314	7.649	7.692	0.249	0.044
10	4.603	4.549	4.577	4.598	4.582	4.607	0.054	0.007	4.576	4.591	0.030	0.015
1	110.155	110.499	110.801	110.569	110.554	110.780	0.344	0.229	110.327	110.676	0.286	0.349
2	156.899	157.110	156.898	156.793	156.800	156.879	0.211	0.092	157.005	156.843	0.152	0.162
3	116.077	119.118	118.825	116.360	116.331	118.838	3.040	2.486	117.598	117.588	2.763	0.009
4	131.509	130.440	130.406	131.485	131.546	130.396	1.069	1.115	130.974	130.958	1.092	0.016
5	113.238	114.993	114.899	113.301	113.203	115.476	1.755	1.935	114.116	114.219	1.845	0.104
6	161.739	159.381	159.221	161.904	161.869	159.201	2.358	2.675	160.560	160.548	2.517	0.011
7	113.370	113.264	113.348	113.512	113.450	112.781	0.107	0.416	113.317	113.273	0.261	0.044
8	129.845	130.166	129.502	129.436	129.599	129.323	0.322	0.105	130.005	129.465	0.213	0.541
1A	135.213	135.917	135.832	134.748	134.857	135.865	0.704	1.045	135.565	135.325	0.875	0.240
4A	128.965	134.287	134.877	128.901	128.998	135.013	5.322	5.996	131.626	131.947	5.659	0.321
5A	147.946	141.587	141.535	147.512	147.461	141.655	6.360	5.891	144.766	144.541	6.125	0.226
8A	126.805	124.653	125.381	127.025	126.890	125.361	2.152	1.586	125.729	126.164	1.869	0.436
9	181.394	180.858	181.019	181.333	181.450	181.049	0.536	0.357	181.126	181.213	0.447	0.087
10	56.390	55.972	56.121	56.360	56.388	56.137	0.418	0.245	56.181	56.251	0.331	0.070

From the last two columns, it is clear that rotation has a much larger effect on chemical shift than stereochemistry. Thus, the NMR spectra at room temperature are dominated by rotational effects, with each peak being slightly "doubled" by stereochemical effects.

Computational Structures:

Calculations were performed using Gaussian 16, revision A.03. Energies are in hartree (at B3LYP-D3(BJ)/6-31G*/PCM(DMSO)). All structures were verified to be local minima or first-order saddle points by frequency analysis as appropriate.

DHA
-765.269653331

C	-3.78253200	-0.30739400	-0.00002200
C	-2.69090800	-1.17708000	-0.00001000
C	-1.38558500	-0.67938800	0.00002000
C	-1.17834100	0.71159400	0.00002200
C	-2.29046600	1.57627300	0.00002100
C	-3.58086700	1.08466400	0.00000900
C	0.17633900	1.29490100	0.00000600
C	1.33174900	0.35840200	0.00002200
C	1.13998000	-1.03288800	-0.00000100
C	2.27190300	-1.85695000	-0.00004100
H	2.14572900	-2.93648600	-0.00006400
C	3.55552000	-1.32363000	-0.00002800
C	3.73483200	0.06861400	-0.00003100
C	2.62320000	0.90288900	-0.00001400
H	-2.85782400	-2.25196300	-0.00002000
H	-2.10596100	2.64499400	0.00003000
H	-4.44234000	1.74420100	0.00002000
H	4.42079500	-1.98199800	-0.00000600
H	2.74410900	1.98000200	-0.00003200
O	0.35213300	2.51792700	-0.00002300
O	4.97155100	0.64952200	0.00008400
H	5.65081800	-0.04431300	-0.00065100
O	-5.06842100	-0.74630400	-0.00006700
H	-5.08058500	-1.71807000	-0.00005800
C	-0.23371700	-1.64972200	0.00011000
H	-0.33177900	-2.31376100	-0.87017700
H	-0.33172100	-2.31347300	0.87062500

DL-gauche⁻
-1529.35526268

C	2.05006000	0.81050100	2.66699100

C	1.60005800	-0.27500300	1.91003300
C	0.28477100	-0.31912400	1.44926800
C	-0.60342100	0.71542900	1.80121000
C	-0.13953700	1.79642500	2.56894600
C	1.17576700	1.85855600	2.99453600
C	-2.02706800	0.66254400	1.41785900
C	-2.52430800	-0.62794400	0.86595800
C	-1.62378700	-1.63423100	0.47719900
C	-2.14177300	-2.83051200	-0.02699200
H	-1.46229300	-3.61859000	-0.34068500
C	-3.51444400	-3.03070100	-0.14238100
C	-4.40302900	-2.01588200	0.24353700
C	-3.90384400	-0.81805800	0.74867400
H	2.29311000	-1.06961300	1.64924800
H	-0.84030700	2.58466900	2.82176700
H	1.54527900	2.69319700	3.58086900
H	-3.89917300	-3.97139400	-0.52838800
H	-4.57934300	-0.02542800	1.04936000
O	-2.78924700	1.61513600	1.60167900
O	-5.75798000	-2.14997300	0.14960500
H	-5.97016400	-3.02348500	-0.21766400
O	3.33308100	0.90641000	3.10305400
H	3.84277900	0.14532300	2.77847500
C	-0.14035400	-1.38610000	0.47752400
H	0.38534400	-2.31923100	0.70154400
C	3.93217300	-2.20809400	-1.02635300
C	2.53599600	-2.19461900	-1.11363800
C	1.83907800	-0.98936200	-1.07444300
C	2.55002100	0.21988900	-0.95117200
C	3.94907700	0.19293000	-0.85270700
C	4.64406500	-1.00485100	-0.88658900
C	1.84700000	1.51776300	-0.90548100
C	0.41095600	1.51374300	-1.29601600
C	-0.28477500	0.30146700	-1.45719700
C	-1.60070000	0.35293300	-1.92723400
H	-2.15534900	-0.56848700	-2.07084000
C	-2.22316800	1.56781000	-2.20059000
C	-1.53190400	2.76967900	-1.99683200
C	-0.21030400	2.73756900	-1.55634800
H	2.00730200	-3.13916800	-1.20142000
H	4.47658900	1.13441300	-0.74494100
H	5.72820400	-1.02019700	-0.81461500
H	-3.24689000	1.58375800	-2.56541600
H	0.34622100	3.65791200	-1.42139000

O	2.43293300	2.56498400	-0.62021900
O	-2.09294800	3.99173100	-2.22982300
H	-3.00900000	3.87394000	-2.53002300
O	4.54764400	-3.41747900	-1.07982300
H	5.50935000	-3.29708800	-1.00889800
C	0.33400500	-0.99816600	-1.02232800
H	-0.04317900	-1.81454100	-1.64536700

DL-gauche+

-1529.35491200

C	-3.93002700	-2.23717900	-1.01105900
C	-2.53326000	-2.21996200	-1.08700500
C	-1.84105400	-1.01192900	-1.05779200
C	-2.55691100	0.19616800	-0.95261000
C	-3.95656900	0.16532000	-0.86526900
C	-4.64721900	-1.03495400	-0.89310900
C	-1.85844800	1.49672600	-0.92131800
C	-0.42262600	1.49292300	-1.31366500
C	0.27712000	0.28105500	-1.45982000
C	1.59151800	0.33047800	-1.93429100
H	2.14883300	-0.59100500	-2.06683200
C	2.20909700	1.54360300	-2.22590100
C	1.51431400	2.74568200	-2.03620700
C	0.19383200	2.71516600	-1.59206700
H	-2.00058600	-3.16356100	-1.15967000
H	-4.48832300	1.10603600	-0.77261300
H	-5.73194700	-1.05316100	-0.83060500
H	3.23178300	1.55825600	-2.59376200
H	-0.36541800	3.63545500	-1.46831600
O	-2.44752100	2.54571300	-0.64879100
O	2.07081500	3.96644700	-2.28664100
H	2.98633400	3.84751600	-2.58798100
O	-4.54091300	-3.44952800	-1.05508600
H	-5.50337700	-3.33160100	-0.99111800
C	-0.33610400	-1.01426200	-1.00492200
H	0.04383100	-1.83806700	-1.61646200
C	-2.03093300	0.84350800	2.68358700
C	-1.58832300	-0.24956700	1.93174600
C	-0.28056000	-0.29609000	1.45628000
C	0.61040100	0.74776400	1.78070200
C	0.15324300	1.83925200	2.53339500
C	-1.15779200	1.90192200	2.97779700
C	2.03134200	0.68976100	1.38764200
C	2.52667400	-0.61238700	0.86214900

```
C    1.62448700   -1.62677300    0.49890400
C    2.14059000   -2.83366500    0.01863800
H    1.45984100   -3.62814400   -0.27562400
C    3.51287400   -3.03659400   -0.09722700
C    4.40296800   -2.01383000    0.26335100
C    3.90573200   -0.80509400    0.74382900
H   -2.29259700   -1.04048000    1.69926900
H    0.85330200    2.63460700    2.76497400
H   -1.50744500    2.75151400    3.55815300
H    3.89609100   -3.98563300   -0.46389400
H    4.58232200   -0.00603100    1.02440800
O    2.79306900    1.64746600    1.54462400
O    5.75764200   -2.15025700    0.16778200
H    5.96837500   -3.03143900   -0.18151600
O   -3.32665300    0.82693000    3.09252100
H   -3.51980500    1.63544900    3.59568300
C    0.14092700   -1.37813400    0.49940000
H   -0.38449300   -2.30730000    0.73966100
```

meso-gauche⁻
-1529.35478937
```
C   -3.74173300   -2.67353100   -0.51987200
C   -2.34860900   -2.57916700   -0.60417200
C   -1.73798700   -1.34602600   -0.81672200
C   -2.53183500   -0.19039500   -0.94578500
C   -3.92714700   -0.29606700   -0.84769600
C   -4.53773900   -1.52155400   -0.63689200
C   -1.91903200    1.13323300   -1.17721700
C   -0.48834700    1.14161600   -1.58877400
C    0.28889700   -0.02742000   -1.49698000
C    1.59365600    0.00566900   -1.99882500
H    2.21081100   -0.88547700   -1.94587800
C    2.12612200    1.16734400   -2.55035800
C    1.35385300    2.33592500   -2.59912300
C    0.04291600    2.31599900   -2.12750900
H   -1.75441400   -3.48141200   -0.49366800
H   -4.52017700    0.60747700   -0.93904500
H   -5.61964400   -1.59800800   -0.56730900
H    3.14280400    1.17060900   -2.93494900
H   -0.57456900    3.20502900   -2.18458200
O   -2.57318900    2.17618900   -1.10359700
O    1.82496600    3.50974600   -3.11177300
H    2.74261300    3.38790400   -3.40514000
O   -4.26925600   -3.90954000   -0.32240500
```

H	-5.23791900	-3.84802500	-0.27977900
C	-0.23696200	-1.23612800	-0.77382100
H	0.20469900	-2.14262100	-1.19837300
C	3.74195400	-2.67336600	0.51976800
C	2.34881800	-2.57908300	0.60395200
C	1.73811300	-1.34600100	0.81660400
C	2.53189300	-0.19034900	0.94591100
C	3.92721900	-0.29593900	0.84794400
C	4.53789200	-1.52136600	0.63702100
C	1.91900400	1.13322000	1.17745000
C	0.48827600	1.14148600	1.58886100
C	-0.28890300	-0.02757500	1.49685100
C	-1.59373300	0.00540500	1.99851900
H	-2.21084800	-0.88575700	1.94537400
C	-2.12631800	1.16699600	2.55011600
C	-1.35409900	2.33560100	2.59912200
C	-0.04310200	2.31578300	2.12767100
H	1.75467800	-3.48134400	0.49327700
H	4.52019600	0.60762100	0.93947200
H	5.61980700	-1.59775700	0.56752900
H	-3.14305200	1.17017700	2.93457000
H	0.57433800	3.20483400	2.18491800
O	2.57313700	2.17621000	1.10410100
O	-1.82532600	3.50934500	3.11184300
H	-2.74300700	3.38743500	3.40507400
O	4.26955600	-3.90932300	0.32218200
H	5.23822000	-3.84775400	0.27965300
C	0.23708300	-1.23617900	0.77361700
H	-0.20454800	-2.14273200	1.19807100

meso-gauche$^+$
-1529.35525686

C	-2.03805300	1.33075500	-2.41415000
C	-1.53419600	0.12139100	-1.92338100
C	-0.22011400	0.03606900	-1.47120300
C	0.61758400	1.16726500	-1.56185600
C	0.09942900	2.37319800	-2.05576800
C	-1.21923500	2.46890400	-2.47078000
C	2.04371900	1.09685600	-1.19128900
C	2.60373000	-0.25907700	-0.93772700
C	1.75357400	-1.36962200	-0.79843000
C	2.33081500	-2.62179400	-0.56925800
H	1.69202800	-3.49334700	-0.45254900
C	3.71138200	-2.77506800	-0.48068200

C	4.54870000	-1.65756100	-0.61438300
C	3.99085500	-0.40236300	-0.84405200
H	-2.19619300	-0.73541900	-1.87401600
H	0.75860900	3.23283000	-2.10936200
H	-1.61609900	3.40727400	-2.84861000
H	4.14215000	-3.75828600	-0.30986500
H	4.62541600	0.47028000	-0.94797800
O	2.75972100	2.10113400	-1.15183600
O	5.90835600	-1.74467100	-0.53304000
H	6.16232800	-2.66856200	-0.37425500
O	-3.33616000	1.34066200	-2.81361900
H	-3.57609700	2.23069000	-3.12113400
C	0.25865200	-1.20500700	-0.76847100
H	-0.21119300	-2.08676100	-1.21426200
C	2.03805300	1.33077400	2.41414300
C	1.53419600	0.12140600	1.92338400
C	0.22011300	0.03608100	1.47120800
C	-0.61758500	1.16727700	1.56185100
C	-0.09942900	2.37321400	2.05575300
C	1.21923400	2.46892400	2.47076300
C	-2.04372000	1.09686400	1.19128800
C	-2.60373000	-0.25907100	0.93773100
C	-1.75357400	-1.36961600	0.79844300
C	-2.33081400	-2.62178900	0.56927600
H	-1.69202700	-3.49334300	0.45257400
C	-3.71138100	-2.77506400	0.48069700
C	-4.54870000	-1.65755600	0.61438900
C	-3.99085600	-0.40235700	0.84405200
H	2.19619200	-0.73540500	1.87402700
H	-0.75860900	3.23284700	2.10934000
H	1.61609900	3.40729700	2.84858500
H	-4.14214900	-3.75828300	0.30988500
H	-4.62541600	0.47028700	0.94797100
O	-2.75972000	2.10114300	1.15181600
O	-5.90835500	-1.74466600	0.53304100
H	-6.16232700	-2.66855800	0.37425900
O	3.33616000	1.34068500	2.81361000
H	3.57609700	2.23071600	3.12111700
C	-0.25865200	-1.20500100	0.76848500
H	0.21119300	-2.08675200	1.21428300

References

1. Goulet, M.-A.; Aziz, M. J., Flow Battery Molecular Reactant Stability Determined by Symmetric Cell Cycling Methods. *J. Electrochem. Soc.* **2018,** *165* (7), A1466-A1477.
2. Goodall, F. L.; Perkin, A. G., LVIII.—Reduction products of the hydroxyanthraquinones. Part V. *J. Chem. Soc, Trans.* **1924,** *125*, 470-476.
3. *RDKit: Open Source Cheminformatic Software*, http://www.rdkit.org/.
4. Stewart, J. J. P. *MOPAC2016, Version: 17.173L*.
5. Tabor, D. P.; Gómez-Bombarelli, R.; Tong, L.; Gordon, R. G.; Aziz, M. J.; Aspuru-Guzik, A., *Theoretical and Experimental Investigation of the Stability Limits of Quinones in Aqueous Media: Implications for Organic Aqueous Redox Flow Batteries*. 2018. ChemRxiv preprint: doi.org/10.26434/chemrxiv.6990053.v2